

# Neutrophil efferocytosis reprograms mitochondrial metabolism to switch alveolar macrophages to a pro-resolution phenotype at the cost of bacterial control

Julian Better<sup>1,2,3,7\*</sup>, Michael Wetstein<sup>1,2,3\*</sup>, Mohammad Estiri<sup>1,2,3</sup>, Christina Malainou<sup>1,2,3</sup>, Maximiliano Ferrero<sup>4,5</sup>, Martin Langelage<sup>1,2,3</sup>, Irina Kuznetsova<sup>1,2,3</sup>, Ivonne Vazquez-Armendariz<sup>1,2,3</sup>, Lucas Kimmig<sup>6</sup>, Siavash Mansouri<sup>2,3,4</sup>, Rajkumar Savai<sup>2,3,4</sup>, Jochen Wilhelm<sup>2,3,7</sup>, Ioannis Alexopoulos<sup>1,2,3</sup>, Natascha Sommer<sup>2,7</sup>, Susanne Herold<sup>+1,2,3</sup>, Ulrich Matt<sup>+#1,2,3</sup>

## Abstract

Resolution of lung injuries is vital to maintain gas exchange. Concurrently, there is an increased risk of secondary bacterial infections. Alveolar macrophages (AMs) are crucial for control of bacterial pathogens and inflammation, but environmental cues that switch these functional phenotypes of AMs remain elusive. Here, we discovered an incapacity of AMs to mount an effective immune response to bacteria during resolution of inflammation. Mechanistically, AM efferocytosis of neutrophils (PMNs), a hallmark of resolution, abrogated mitochondrial ROS (mtROS) production upon bacterial encounter. PMN-derived myeloperoxidase (MPO) fueled canonical glutaminolysis via uncoupling protein 2 (UCP2), which resulted in decreased mtROS dependent killing of bacteria and secretion of pro-inflammatory cytokines. Instead, MPO-enhanced UCP2 expression inhibited mitochondrial hyperpolarization and boosted efferocytosis irrespective of the presence of bacterial pathogens. Overall, uptake of apoptotic PMNs switches AMs to prioritize resolution of inflammation over antibacterial responses and similarly affects murine macrophages at extra-pulmonary sites, and human AMs.

## Affiliations:

1 Department of Medicine V, Internal Medicine, Infectious Diseases and Infection Control, Universities of Giessen and Marburg Lung Center (UGMLC), member of the German Center for Lung Research (DZL), Justus-Liebig University (JLU) Giessen, Giessen, Germany

2 Cardio-Pulmonary Institute (CPI), Giessen, Germany

3 Institute for Lung Health (ILH), Giessen, Germany

4 Department of Lung Development and Remodeling, Max-Planck Institute for Heart and Lung Research, Bad Nauheim, Germany

5 Biomedicine Research Institute of Buenos Aires - CONICET-Partner Institute of the Max Planck Society (IBioBA-MPSP) Buenos Aires, Argentina

6 University of Chicago Medicine Chicago, Illinois

7 Department of Internal Medicine II, Pulmonary & Critical Care, UGMLC, member of the DZL, JLU, Giessen, Germany

\* shared first authors

+ senior authors, # corresponding author: [ulrich.matt@innere.med.uni-giessen.de](mailto:ulrich.matt@innere.med.uni-giessen.de)

## Introduction

Tissue-resident macrophages (TRMs) regulate induction and resolution of inflammation by release of cytokines or chemokines, pathogen clearance, and promoting resolution of inflammation (e.g., by removal of apoptotic cells) (Davies et al., 2013). Thus, TRMs must swiftly adapt anti- and pro-inflammatory properties with the ultimate goal to restore homeostasis. In the alveoli and larger airways, AMs are the sentinel cells essential for homeostasis, resolution of inflammation, and clearance of bacteria (Green and Kass, 1964; Hussell and Bell, 2014; Neupane et al., 2020). After lung injuries, restoration of proper gas exchange is vital and requires rapid clearance of apoptotic PMNs by AMs (Grabiec and Hussell, 2016; Matthay et al., 2012; Schneider et al., 2014). In macrophages in general, efferocytosis (i.e. the uptake of apoptotic cells by macrophages) has been shown to induce an anti-inflammatory profile characterized by secretion of IL-10 and TGF- $\beta$  (Fadok et al., 1998; Voll et al., 1997), further enhance clearance of dead cells (Park et al., 2011), promote organ repair (Chang et al., 2018; Horckmans et al., 2017; Zhang et al., 2019), and decrease antibacterial properties (Medeiros et al., 2009). Thus, the net benefit of improved resolution might coincide with an impaired ability to fend off bacterial pathogens. Secondary bacterial infections are common in community-acquired (CAP) and nosocomial pneumonia, and AMs are implicated herein (Kaur et al., 2015). Respiratory viruses, which are leading causes of CAP (Jain et al., 2015), predispose to bacterial superinfections (Morens et al., 2008; Morgan et al., 2018), and gastric aspiration was shown to be the strongest independent risk factor for pneumonia in intubated patients (Cook et al., 1998; Metheny et al., 2006). Thus, the exploration of mechanisms that govern antibacterial and pro-resolving functions of AMs is of clinical importance. However, whether these opposing macrophage effector functions are under control of a common upstream signaling hub that controls switch of effector functions, and the involved cellular compartments and molecular events, remained incompletely understood.

We observed earlier that acid aspiration leads to uncontrolled bacterial outgrowth in secondary bacterial pneumonia (Matt et al., 2009). In this model, administration of an anti-inflammatory compound during acid aspiration restored bacterial control by AMs. Thus, inflammation or the resolution thereof affects antibacterial properties of AMs, but the mechanism and meaning of this functional alteration remained unresolved.

Here, we set out to explore functional properties of AMs during inflammation and untangle mechanisms that regulate functional fate decisions of AMs *in vivo*. By combining *in vivo* with functional *ex vivo* as well as *in vitro* analyses, we ultimately revealed that during resolution of inflammation, AMs have impaired antibacterial but improved pro-resolving properties. Mechanistically we found that efferocytosis of neutrophils rewires mitochondrial metabolism via UCP2 in an MPO-dependent manner, which impaired mtROS production in response to bacteria. At the same time, UCP2 upregulation further enhanced efferocytosis by AMs even in

the presence of bacteria, pointing at a feedforward mechanism. MPO-induced reprogramming of macrophages similarly occurred in viral pneumonia, and across bacterial pathogens and different macrophage subsets, including human AMs (hAMs). Thus, increased UCP2 expression consecutive to PMN efferocytosis represents a conserved immunometabolic decision point that restricts the functional plasticity of TRMs to prioritize resolution of inflammation over host defense against bacteria.

## Results

### AMs exhibit a transient impairment of antibacterial responses along with increased oxidative phosphorylation during resolution of sterile pneumonitis

To explore the functional polarization of AMs during the course of pulmonary inflammation, we used a mouse model of acid aspiration (Matt *et al.*, 2009). At different time points after intratracheal instillation of hydrochloric acid (HCl), ranging from 12 hours to 8 days, mice were either infected with *Pseudomonas aeruginosa* (*P. aeruginosa*), or AMs were harvested for *ex vivo* analysis (Figure 1A). For *in vivo* infection, the bacterial load was quantified at an early time point of infection where *de novo* PMN recruitment is negligible, and thus AMs are the predominant leukocytes to clear bacteria. While bacterial outgrowth was low in most animals, those that received acid 24 hours before exhibited a significantly increased bacterial burden (Figure 1B). At that time resolution of acid-induced inflammation took place, as PMN numbers were in sharp decline (Figure 1C). Recruitment of monocyte-derived macrophages (MDMs) peaked at 96 hours at relatively low levels (Figure 1D), indicating that tissue-resident AMs are the primary macrophage subset present during resolution of acid-induced inflammation (gating strategy, Figure S1B). To correlate the *in vivo* susceptibility to bacterial infection to AM function, we isolated AMs at the same time points as we infected mice *in vivo* and analyzed the bactericidal properties of these cells *ex vivo*. As total AM counts drop during the course of inflammation (Figure 1D), we normalized AM numbers for *ex vivo* experiments. Matching our *in vivo* data, AMs taken from mice 24 hours after acid aspiration were most significantly impaired in bacterial killing (Figure 1E). Next, we performed a transcriptome analysis of flow-sorted AMs after acid aspiration with and without bacterial infection using the same experimental setup (Figure 1A). Analysis of selected pro-inflammatory marker genes such as *Tnf- $\alpha$* , *Il-6*, *Il-1 $\beta$* , *Cxcl2*, and Toll-like receptors (*tlrs*) illustrates an impaired response to bacteria 24 hours after acid aspiration in AMs (Figure 1F), which was similarly found in KEGG (Kyoto Encyclopedia of Genes and Genomes)-pathway analysis of NF $\kappa$ B-, and TNF-signaling (Figure S1C and S1D). At later time points after instillation of acid, a pro-inflammatory response recurred (Figure 1F). Thus, 24 hours after acid aspiration AMs are less responsive to a bacterial challenge. Notably, the most significantly altered pathway ( $p=-\log 14.5$ ) in the KEGG analysis in all comparisons performed was oxidative phosphorylation (OXPHOS) between AMs of mice that underwent acid aspiration 24 hours before infection and AMs from animals that were solely infected (Figure 1G for metabolic pathways and 1H for OXPHOS genes). To test if transcriptional changes mirror functional properties, we performed *ex vivo* extracellular flux analysis. Basal and maximal respiration were increased in response to bacteria in AMs of animals that underwent acid aspiration 24 hours before compared to sham-treated animals and those that received acid 8 days before (Figure 1I), linking transcriptional regulation to mitochondrial function. At the same time, AMs retrieved 24 hours after acid aspiration showed

a clearly diminished extracellular acidification rate (ECAR) when challenged with bacteria compared to sham treatment (Figure 1J). Thus, AMs exhibit a transiently impaired response to bacteria, paralleled by increased oxygen consumption rate (OCR).

### **Production of mtROS is impaired during resolution of inflammation in AMs upon bacterial encounter**

During OXPHOS mitochondria produce mtROS (Brand, 2010), which is a crucial process in bacterial killing (Hall et al., 2013; West et al., 2011). Therefore, we tested the capacity of acid-experienced vs sham-treated AMs to produce mtROS in response to *P. aeruginosa ex vivo*. AMs harvested 24 hours after acid aspiration failed to mount mtROS production upon bacterial stimulation, whereas after 8 days mtROS release recurred was partially restored (Figure 2A). In contrast, cytosolic ROS production (cROS) remained intact in AMs of mice that underwent acid aspiration (Figure 2B). Flux through the electron transport chain (ETC) gives rise to a basal amount of mtROS release. An increased mitochondrial membrane potential (MMP) results in enhanced mtROS production and may limit electron flux, oxygen consumption, and ATP production under certain conditions (Berry et al., 2018). As such, the MMP was shown to be a driving force for the generation of mtROS (Zorova et al., 2018), and to be required for mtROS release in response to LPS (Mills et al., 2016). Accordingly, AMs from mice that underwent acid aspiration 24 hours before failed to increase the MMP upon bacterial stimulation *ex vivo*, whereas AMs from sham-treated animals or from mice that underwent aspiration 8 days before responded with an increase of the MMP (Figure 2C). Confirming the importance of mtROS for bacterial control, the mtROS scavenger MitoTEMPO reduced intracellular bacterial killing in AMs from sham-treated animals and from mice that had received acid 8 days or 12 hours before but did not alter AM clearance capacity at 24 hours after acid aspiration *ex vivo* (Figure 2D). Apart from affecting bactericidal properties, mtROS were shown to impact the secretion of cytokines (Naik and Dixit, 2011). First, we tested the cytokine secretion of AMs primed during acid aspiration *in vivo* in response to *P. aeruginosa ex vivo*. Matching the transcriptome data (Figure 1F), AMs from mice that underwent acid aspiration 24 hours before exhibited a significant decrease in the production of the pro-inflammatory cytokines IL-1 $\beta$ , IL-6, and TNF- $\alpha$  (Figure 2E). Scavenging of mtROS in AMs markedly diminished secretion of IL-1 $\beta$ , and at least partially reduced IL-6 release, whereas TNF- $\alpha$  release was unaffected (Figure S2). Vice versa, the anti-inflammatory cytokine IL-10 was highest upon stimulation with *P. aeruginosa* when acid had been applied 24 hours before (Figure 2F). Thus, AMs have a profound defect in generating mtROS and mtROS-dependent (IL-1 $\beta$  and IL-6), and -independent (TNF- $\alpha$ ) cytokines in response to bacteria during resolution of inflammation, while IL-10 secretion is enhanced.

### **Efferocytosis of PMNs leads to increased oxygen consumption and precludes mtROS release in response to bacteria in AMs**

Next, we aimed to delineate the alveolar cues that switch AMs towards an impaired bacterial response during resolution of acid-induced pneumonitis. To test the role of soluble alveolar mediators, we incubated cell-free bronchio-alveolar lavage fluid (BALF) harvested at different time points after acid aspiration with AMs but could not reproduce an impaired mtROS release in response to bacteria (Figure S3A). Cellular composition of BALF after acid aspiration revealed increased levels of apoptotic epithelial cells (main constituent of CD45<sup>neg</sup> cells) and apoptotic PMNs peaking at around 12 to 24 hours (Figure 3A). To assess their potential impact on mtROS production, apoptosis in alveolar epithelial cells (AECs) and PMNs was induced with staurosporine to similar levels (Figure S3B). Whereas uptake of apoptotic AECs by AMs did not affect release of mtROS, ingestion of apoptotic PMNs significantly impaired mtROS production upon bacterial stimulation with *P. aeruginosa* *in vitro* (Figure 3B). Accordingly, AM efferocytosis of PMNs, but not of AECs, prevented an increase of the MMP (Figure 3C) in response to and diminished bacterial killing of *P. aeruginosa* (Figure 3D). Matching the *ex vivo* data (Figure 2D), scavenging of mtROS did not further reduce the bacterial killing capacity of AMs after ingestion of apoptotic PMNs *in vitro* (Figure 3E). Of note, ingestion of apoptotic PMNs had no impact on cROS release upon bacterial encounter (Figure S3C). In line with reduced mtROS release, cytokine release by AMs was completely (IL-1 $\beta$ ) or partially (IL-6) diminished after PMN efferocytosis and consecutive bacterial challenge (Figure 3F). Uptake of apoptotic AECs slightly reduced IL-6 levels, whereas uptake of either apoptotic AECs or PMNs blunted TNF- $\alpha$  release in response to *P. aeruginosa* (Figure 3F). Of note, significant baseline IL-10 secretion was detected after efferocytosis of AECs and PMNs by AMs without prior bacterial stimulation (Figure S3D). In contrast, *P. aeruginosa*-treated AMs released IL-10 only after PMN efferocytosis (Figure 3G). Taken together, our data suggest that the effects of efferocytosis on the functional phenotype of AMs are cell-type specific. PMN but not AEC ingestion blunted mtROS release in AMs after bacterial challenge, which ultimately impaired bacterial killing and diminished secretion of pro-inflammatory cytokines, while IL-10 secretion was enhanced. Overall, PMN efferocytosis reprograms AMs to blunt mtROS release in response to bacteria.

### **PMN-derived MPO mediates immunometabolic alterations upon efferocytosis in AMs in response to bacteria**

We next sought to identify the PMN component accounting for efferocytosis-driven immunometabolic alterations in AMs impairing mtROS generation and bactericidal functions. As a major constituent of PMN granules are enzymes mediating antimicrobial functions, we tested lipocalin-2 (NGAL), elastase, and MPO for their ability to inhibit mtROS production upon bacterial stimulation in AMs. Whereas elastase and NGAL-treated AMs maintained their capacity to mount mtROS, pre-incubation with MPO abrogated mtROS production in response to *P. aeruginosa* (Figure 4A). Of note, the concentration of MPO (0.5 $\mu$ M) used did not affect

the viability of AMs (Figure S4A), and mitochondrial content was not altered by MPO treatment (Figure 4B). To elucidate MPO's impact in the context of efferocytosis, we incubated AMs with apoptotic PMNs of either wildtype (WT) or *Mpo*<sup>-/-</sup> animals. MPO deficiency clearly restored the capacity of AMs to build mtROS (Figure 4C) and led to an increase of the MMP after efferocytosis in response to bacteria (Figure 4D). Accordingly, the killing capacity improved significantly after incubation with PMNs lacking MPO compared to WT PMNs (Figure 4E). Extracellular flux analysis of AMs that had ingested *Mpo*<sup>-/-</sup> PMNs abrogated an increase in oxygen consumption compared to WT PMNs when challenged with bacteria, further confirming that heightened OXPHOS dampens antibacterial responses (Figure 4F). To address the relevance of our findings *in vivo*, we instilled apoptotic PMNs intratracheally and subsequently infected the mice with *P. aeruginosa* (Figure 4G). According to our *in vitro* results, a lack of MPO in PMNs improved bacterial clearance compared to WT PMNs *in vivo* (Figure 4H). Of note, PMN efferocytosis diminishes bacterial killing partially independently of MPO (Figure 4E+H). Thus, additional mechanisms such as prostaglandin E-2 mediated inhibition of bacterial killing as previously reported most likely play a role (Medeiros *et al.*, 2009). To examine if MPO attenuation of bacterial control is a pathogen-specific effect, we tested *Klebsiella pneumoniae* (*K. pneumoniae*) and *S. pneumoniae* in this experimental setting. Elimination of both pathogens was diminished by preincubation with MPO *in vitro* (Figure 4I). In line, efferocytosis of PMNs and not AECs prevented generation of mtROS in response to *S. pneumoniae* (Figure S4B). Likewise, mtROS release was attenuated in response to *K. pneumoniae* after MPO pre-treatment (Figure 4J). Taken together, PMN MPO, likely unleashed during the efferocytosis process abrogates mtROS release and increases oxygen consumption in response to bacteria in AMs.

### **MPO increases UCP2 expression, which mediates inhibition of mtROS generation upon bacterial encounter**

Clearance of apoptotic PMNs rendered AMs unable to increase the MMP and consecutively the release of mtROS upon bacterial encounter while enhancing oxygen consumption. Uncoupling proteins (UCPs) were found to dissipate the proton gradient across the inner mitochondrial membrane resulting in decreased MMP and mtROS production (Berry *et al.*, 2018; Brand and Esteves, 2005). To test if UCP2, which is expressed in macrophages (Fleury *et al.*, 1997) and AMs (Steer *et al.*, 2013), is implicated in MPO-induced mitochondrial targeting, we used the UCP2 inhibitor genipin. After MPO treatment, genipin rescued mtROS production in AMs stimulated with bacteria *in vitro* (Figure 5A). In line, incubation with genipin restored mtROS release of AMs isolated 24 hours after acid aspiration and challenged with bacteria *ex vivo* (Figure 5B). Next, we used *Ucp2*<sup>-/-</sup> AMs, exposed them to apoptotic WT PMN for efferocytosis *in vitro* and found them to still respond with mtROS production when challenged with bacteria (Figure 5C). Accordingly, in *Ucp2*<sup>-/-</sup> AMs, MPO pretreatment did not preclude an

increase of the MMP in response to bacteria (Figure 5D) and did not diminish bacterial killing *in vitro* (Figure 5E). Furthermore, the OCR did not rise in response to bacteria after MPO treatment in AMs deficient in UCP2 (Figure 5F). Regarding cytokine secretion, inhibition of UCP2 using genipin restored the release of IL-1 $\beta$  and IL-6, but not TNF $\alpha$  in AMs of WT mice pretreated with MPO *in vitro* (Figure S5A), whereas secretion of IL-10 was not affected (Figure S5B). Thus, MPO-mediated effects on mtROS release after bacterial encounter in AMs depend on UCP2 function. Therefore, we speculated that MPO might affect UCP2 levels in AMs. While we did not detect alterations in transcriptional regulation during inflammation *in vivo* or after efferocytosis and secondary bacterial stimulation *in vitro* (Figure S5C), protein levels of UCP2 were increased in AMs harvested 24 hours after acid aspiration compared to sham-treated animals (Figure 5G). In line, *in vitro* stimulation of AMs with MPO increased the expression of UCP2 (Figure 5H). To demonstrate the relevance of our findings *in vivo*, we treated mice 24 hours after acid aspiration with genipin or carrier control intratracheally and subsequently infected them with *P. aeruginosa* (Figure 5I). Confirming our *ex vivo* and *in vitro* data, mice that received genipin exhibited a significantly lower bacterial burden in the BALF compared to control animals (Figure 5J). Of note, genipin did not impair bacterial growth itself (Figure S5D). Together, these data reveal that PMN-derived MPO increases UCP2 expression in AMs, which augments oxygen consumption and precludes infection-induced mtROS release and bacterial killing *in vitro* and *in vivo*.

### **MPO-induced UCP2 expression drives canonical glutaminolysis in response to bacteria**

Emerging evidence highlights the role of UCP2 as a metabolic hub that determines the relative contribution of substrates being oxidized by mitochondria (Bouillaud, 2009; Pecqueur et al., 2009; Rupprecht et al., 2019; Voza et al., 2014). More precisely, UCP2 is implicated in favoring the oxidation of fatty acids and glutamine while limiting the oxidation of glucose-derived pyruvate (Figure 6A). In macrophages, UCP2 has been shown to promote the efficient mitochondrial oxidation of glutamine (Nubel et al., 2008). Since MPO pre-treatment led to an increase of the OCR via UCP2 after bacterial stimulation, we wondered whether specific fueling of the tricarboxylic acid (TCA) cycle is implicated herein. Investigating the maximum mitochondrial respiration in presence of pathway-specific inhibitors (substrate oxidation stress test) revealed a relative increase in glutaminolysis and conversely, a relative decrease in glycolysis in AMs when treated with *P. aeruginosa* plus MPO compared to *P. aeruginosa* alone, whereas fatty acid oxidation remained unchanged (Figure 6B). In fact, inhibition of glutaminolysis by BPTES, an inhibitor of glutaminase-1, completely blunted an increase in the OCR in response to MPO and bacteria *in vitro* (Figure 6C). Accordingly, inhibition of glutaminolysis abrogated inhibition of mtROS production after incubation with MPO and bacteria (Figure 6D). In line, the inhibitory effect of PMN efferocytosis on the release of the mtROS-dependent cytokine IL-1 $\beta$  in response to bacteria was partially abolished after

inhibition of glutaminolysis (Figure 6E), while IL-10 secretion was slightly but significantly reduced (Figure 6F). Canonical glutaminolysis relies on the enzymatic activity of glutamate dehydrogenase (GLUD1), which converts glutamate into  $\alpha$ -ketoglutarate ( $\alpha$ -KG) to fuel the TCA cycle. Incubation of AMs with MPO and the GLUD1-inhibitor epigallocatechin gallate (EGCG) restored mtROS release (Figure 6G), and the increase of the MMP (Figure 6H) in response to *P. aeruginosa*. Dimethyl- $\alpha$ -KG (DM- $\alpha$ -KG) is a cell-permeable analog of  $\alpha$ -KG. Treatment of AMs with genipin plus DM- $\alpha$ -KG restored the MPO-mediated inhibition of mtROS secretion (Figure 6I), enabled an increase of the MMP in response to bacteria (Figure 6J), and normalized the capacity to kill bacteria (Figure 6K). Together, MPO-induced UCP2 expression enhances the efficient oxidation of glutamine via canonical glutaminolysis in the presence of bacteria. Consequently, AMs are unable to release mtROS, which impairs bacterial killing and affects mtROS-dependent cytokine release.

### **MPO primes different macrophage subsets to blunt bacterial response**

Next, we wanted to investigate, if MPO-induced alterations are restricted to AMs or also apply to macrophages of extra-pulmonary sites. As in AMs, efferocytosis of PMNs but not AECs by primary peritoneal macrophages (PMs) and bone-marrow derived macrophages (BMDMs) resulted in decreased mtROS production (Figure 7A), an unaltered MMP (Figure S6A) in response to, and an impaired killing of *P. aeruginosa* (Figure 7B), while cROS secretion remained unaffected *in vitro* (Figure S6B). In line, MPO increased UCP2 expression in both macrophage subsets (Figure S6C), and metabolic analysis demonstrated an increase in glutaminolysis-dependent oxygen consumption after MPO pre-treatment in response to bacteria in both PMs and BMDMs while the contribution of glycolysis- and fatty acid oxidation to mitochondrial oxygen consumption remained unaltered by MPO treatment (Figure S6D). Furthermore, mtROS production was unaffected after MPO incubation and challenge with *P. aeruginosa* in *Ucp2*<sup>-/-</sup> BMDMs and PMs (Figure 7C). Neutrophil efferocytosis also drastically diminished IL-1 $\beta$  secretion in PMs and BMDMs stimulated with bacteria (Figure S6E), suggesting a conserved mechanism among macrophages of different ontogeny and tissues. As in AMs, IL-6 secretion was inhibited after PMN efferocytosis and BMDMs upon bacterial stimulation (Figure S6E). IL-10 secretion was detected already after bacterial stimulation alone but further increased after efferocytosis of PMNs in PMs but was not affected by efferocytosis in PMs and BMDMs in response to *P. aeruginosa* (Figure S6F). Next, we tested human primary AMs (hAMs) taken from BALF of patients with uninflamed lungs. Like murine macrophages, hAMs failed to produce mtROS in response to bacteria after MPO stimulation, and genipin prevented MPO-mediated impairment of mtROS generation, whereas  $\alpha$ -KG restored MPO-mediated effects in the presence of genipin (Figure 7D). Moreover, IL-1 $\beta$  secretion was reduced in response to bacteria after MPO pre-treatment, whereas IL-6 was not affected

(Figure S6G). Thus, MPO is a conserved signal in macrophages across species to blunt antibacterial responses via UCP2.

### **MPO boosts PMN efferocytosis in different macrophage subsets while limiting bacterial control *in vivo***

Efferocytosis as such promotes the uptake of apoptotic cells, which has been referred to as “continued efferocytosis” (Gerlach et al., 2021; Wang et al., 2017; Yurdagul et al., 2020). In line, we found that AMs exhibited an increased capacity to ingest apoptotic PMNs during resolution of inflammation (i.e., 24 hours after instillation of acid) (Figure 7E). UCP2 was shown to decrease the MMP to enhance the continued clearance of apoptotic cells in macrophages (Park *et al.*, 2011); therefore, we tested the impact of cell-type specific efferocytosis in the context of an altered MMP due to bacterial stimulation. As expected, efferocytosis of both PMNs and AECs enhanced the uptake of apoptotic PMNs in a second round of efferocytosis in AMs (Figure 7F, blue bars). In contrast, stimulation with bacteria after the first round of efferocytosis with AEC and in control AMs (no efferocytosis) reduced ingestion of apoptotic PMNs in the second or first round, respectively (Figure 7F, red bars). In contrast to this, PMN efferocytosis caused a feed-forward loop of continued efferocytosis despite the presence of bacteria, as evidenced by a sustained efferocytosis level in the second round (Figure 7F, “PMN” red bar). Since MPO alone increases UCP2 expression and lowers the MMP (Figure S6H), we speculated that MPO might foster continued efferocytosis. Indeed, MPO alone mimicked the effects of PMN efferocytosis in the presence of bacteria during the second round of ingestion of apoptotic cells (Figure 7G). Importantly, *Ucp2*<sup>-/-</sup> AMs did not enhance efferocytosis in response to MPO (Figure 7H). Murine PMs and BMDMs (Figure S6I) as well as hAMs (Figure 7I) similarly increased the ingestion of apoptotic PMNs after MPO treatment. To corroborate our findings *in vivo*, we performed acid aspiration followed by secondary bacterial infection with *P. aeruginosa* for 10 hours with or without i.t. pre-treatment with genipin (Figure 7J). In line with our *in vitro* and *ex vivo* findings, pre-treatment with genipin increased the number of apoptotic cells per lung surface compared to controls (Figure 7K), and overall inflammation was higher in genipin-treated mice that had impaired resolution of inflammation (Figure S6J). To test the relevance of our findings on disease outcome in clinically relevant models, we performed second-hit models using acid aspiration or IAV infection as a first hit, and secondary bacterial infection with *P. aeruginosa* or *S. pneumoniae*, respectively as a second hit (Figure 7J and Figure 7M). Genipin pre-treatment restored bacterial control during secondary *P. aeruginosa* infection after acid aspiration (Figure 5I), and improved survival in the same model (Figure 7L). Similarly, genipin pre-treatment strongly reduced the bacterial load when mice were superinfected with *S. pneumoniae* during IAV pneumonia (Figure 7N), and consequently improved survival in this model (Figure 7O).

In summary, our data reveal that PMN efferocytosis rewires mitochondrial metabolism by an MPO-UCP2 signaling hub in macrophages to switch their phenotype and prioritize resolution of inflammation over bacterial control, resulting in fatal outcome in secondary bacterial infections. These findings were conserved across species, macrophage subsets, and bacterial pathogens.

## Discussion

AMs and macrophages are generally appreciated as orchestrators of inflammation by swiftly adapting functional phenotypes according to the microenvironment they reside in. Accordingly, they might polarize towards a pro-resolution and anti-inflammatory or a pro-inflammatory and bactericidal state. The underlying mechanisms and consequences in clinically relevant pneumonia models have not been systematically studied so far.

Here, starting from an unbiased *in vivo* approach, we revealed that PMN efferocytosis locks macrophages in a pro-resolution state, which impairs antibacterial responses. *In vivo*, this translates into impaired control of bacteria during resolution of inflammation in acid aspiration and influenza pneumonia. Murine and human tissue-resident macrophages of the lung and the peritoneum exhibited similar responses after ingestion of apoptotic PMNs, or PMN-derived MPO, *in vitro*. Thus, MPO-induced mitochondrial reprogramming by UCP2 constitutes a conserved checkpoint during inflammation to switch macrophages to a pro-resolution phenotype at the expense of bacterial control.

Over the last years, an increasing number of elegant research unveiled metabolic consequences of efferocytosis in macrophages (Merlin et al., 2021; Morioka et al., 2018; Trzeciak et al., 2021; Yurdagul *et al.*, 2020; Zhang *et al.*, 2019). However, the metabolic pathways regulating the innate immune response of macrophages after efferocytosis remained largely unknown. We detected increased UCP2 expression after efferocytosis of PMNs, which led to enhanced oxygen consumption fueled by canonical glutaminolysis in response to bacteria. This metabolic rewiring precluded a rise in the MMP and mtROS release in response to bacteria. The exact mechanism by which UCP2 modulates the MMP and mtROS production remains an open question, and available data are controversial. UCP2 was reported to have mild uncoupling properties by increasing proton conductance of the inner mitochondrial membrane of the respiratory chain upon specific activation, diminishing mtROS release (Arsenijevic et al., 2000; Brand and Esteves, 2005). However, a mounting body of evidence highlights the role of UCP2 as a metabolic carrier (Bouillaud, 2009; Cannon et al., 2006; Pecqueur *et al.*, 2009). UCP2 was demonstrated to export C4 metabolites out of mitochondria, thereby limiting the oxidation of acetyl-CoA-producing substrates such as glucose and favoring glutaminolysis (Vozza *et al.*, 2014). By exporting C4 compounds from mitochondria, UCP2 reduces the redox pressure on the ETC and hereby, mtROS release (Vozza *et al.*, 2014). Here, we show that in macrophages, enhanced UCP2 expression by MPO precludes a hyperpolarized MMP and consecutive mtROS release in response to bacteria, which is reversible by inhibition of canonical glutaminolysis. Furthermore, a mitochondrial substrate oxidation stress test of AMs responding to bacteria after prior efferocytosis compared to infection alone revealed that mitochondrial oxygen consumption was fueled by glutaminolysis while the contribution of glycolysis was being limited. Therefore, we suggest that metabolic

regulations by UCP2 are crucial in this context. At the same time, enhanced UCP2 expression facilitates further efferocytosis supporting resolution of lung inflammation. Improved efferocytosis after ingestion of apoptotic cells, a phenomenon termed *continued efferocytosis* is a well-established process (Doran et al., 2020). Both, ingestion of apoptotic PMNs and AECs enhanced continued efferocytosis *in vitro*. However, AMs that had ingested AECs exhibited a “back to baseline” efferocytic capacity in the presence of bacteria. In contrast, PMN efferocytosis led to an increased efferocytic capacity of AMs even upon bacterial encounter in an MPO-dependent manner. Our data not only support the overall concept that PMN efferocytosis initiates and drives resolution of inflammation (Fullerton et al., 2013; Peiseler and Kubes, 2019; Serhan and Savill, 2005) but furthermore reveal that ingestion of apoptotic PMNs prioritizes continued efferocytosis over antibacterial responses in macrophages. This functional fate decision makes sense, given that accrual of necrotic PMNs can promote inflammation and tissue damage (Bratton and Henson, 2011; Morioka et al., 2019), but in some instances, comes at the cost of severe gram-negative or gram-positive pneumonia. Intriguingly, MPO in PMNs was found to protect mice during sterile endotoxemia, but the mechanism remained elusive (Reber et al., 2017). In yet another interesting study, Faas et al. recently discovered that UCP2 promotes repair mechanisms in macrophages in response to the alarmin IL-33 in a model of muscle injury (Faas et al., 2021). Thus, different danger signals (i.e., MPO, IL-33) increase UCP2 expression to improve resolution properties of macrophages. UCP2 might therefore constitute an important signaling hub to promote a repair/pro-resolution phenotype in macrophages in various settings. We speculate that our findings might be applicable to most disease states where PMN efferocytosis occurs, but this remains to be investigated in further, relevant experimental models of tissue inflammation and injury.

The induction of an anti-inflammatory phenotype in macrophages upon efferocytosis was first described almost 25 years ago (Fadok et al., 1998; Voll et al., 1997). Efferocytosis was shown to inhibit NF $\kappa$ B- and TLR-engagement to block pro-inflammatory signaling pathways (Elliott et al., 2017). In line, in the current study, pro-inflammatory responses in both pathways were diminished upon infection with *P. aeruginosa* compared to sham-treated animals *in vivo* during resolution of acid-induced pneumonitis. Importantly, transcriptional regulation and secretion of cytokines *in vivo* and *ex vivo* were largely mimicked by efferocytosis *in vitro*. While ingestion of apoptotic AECs strongly restricted TNF- $\alpha$  production, clearance of apoptotic PMNs further inhibited IL-1 $\beta$  and partially IL-6 secretion in response to bacteria. Accordingly, scavenging of mtROS strongly diminished IL-1 $\beta$  and to a lesser extent IL-6 secretion, whereas TNF- $\alpha$  was not affected upon bacterial encounter in AMs. Mitochondrial ROS were previously reported to trigger IL-1 $\beta$  release via inflammasome activation (Zhou et al., 2011), and to promote activation of Mitogen-activated protein kinases (MAPKs) supporting IL-6 secretion (Naik and Dixit, 2011). Recently, Billingham et al. demonstrated NLRP3 inflammasome activation by LPS depended

on the ETC function, but was independent of mtROS (Billingham et al., 2022). The dependency of IL-1 $\beta$  release on mtROS as observed by us and others (Mills *et al.*, 2016; Zhou *et al.*, 2011) can be explained by using whole bacteria instead of cell wall components altering quality or kinetics of the response, or by other inflammasomes involved in caspase activation. Upon bacterial stimulation, IL-6 levels were consistently diminished in settings of reduced mtROS release in AMs and BMDMs, but not in murine PMs and hAMs, manifesting cell-type and species-specific differences. Previously, scavenging or reduction of mtROS had protective effects in LPS-endotoxemia (Lowes et al., 2008; Mills *et al.*, 2016) and influenza pneumonia (To et al., 2020) by limiting the release of pro-inflammatory cytokines and reducing apoptosis and necrosis of PMNs.

In contrast, IL-10 secretion was not influenced by MPO but was observed after PMN efferocytosis upon bacterial encounter. The mechanism of enhanced, anti-inflammatory IL-10 release in this setting remains to be investigated. However, this effect is consistent with the overall notion that PMN efferocytosis primes for resolution of inflammation, while limiting pro-inflammatory responses in the presence of bacteria. Overall, we found a conserved effect of PMN efferocytosis on immune functions, causing a shift from pro- to anti-inflammatory cytokines.

In summary, we delineated a conserved mechanism of MPO-dependent mitochondrial metabolism reprogramming that restricts the functional plasticity of macrophages to prioritize tissue-protective properties. While this is advantageous in most circumstances, it creates a window of opportunity for bacterial outgrowth during the resolution of inflammation, which might result in severe gram-negative pneumonia after aspiration or gram-positive pneumonia after viral infection. Considering an increasing number of clinical studies that evaluate the therapeutic potential of cell therapies using apoptotic cells (Poon et al., 2014; Saas et al., 2016; Toussiot et al., 2021; van Heerden et al., 2021), and a recent trial to alleviate the inflammatory response in SARS-CoV-2 pneumonia using apoptotic peripheral blood monocytes (Enlivex Therapeutics Ltd., 2021), our results stress the importance to discern the effects of different apoptotic cell preparations on macrophages. Furthermore, we suggest that modulation of canonical glutaminolysis or UCP2 inhibition might constitute a therapeutic approach to instruct macrophages for improved host defense functions after aspiration or during viral pneumonia.

### **Limitations of the study**

Results on the MPO/UCP2-axis were consistent across all models applied (*in vitro*, *ex vivo*, *in vivo*). However, we did not perform genetic deletion studies of these proteins during the first hit (e.g. IAV infection, acid pneumonitis) to study their impact on secondary bacterial infections *in vivo*, because deletion of these crucial molecules in leukocytes was previously reported to alter the course of inflammations such as LPS-pneumonitis or influenza pneumonia. Therefore,

results of second hit models after genetic deletion of *Ucp2* or *Mpo* will be confounded by differences of the inflammation during the first hit.

### **Acknowledgments**

We thank Larissa Hamann, Stefanie Jarmer, Florian Lück, and Julia Stark for their excellent technical assistance. We are grateful to Sylvia Knapp for critically reading the manuscript, and Elena Pohl for fruitful discussions.

### **Author contributions**

J.B., and M.W. designed the study, performed experiments, interpreted results, and wrote the manuscript. M.E., C.M., M.F., M.L., I.K., and S.M. performed experiments, collected data, and interpreted results. I.V.-A., L.K., R.S., and N.S. conceptualized experiments, and provided essential material. J.W. performed bioinformatics analysis and interpreted the data. I.A. performed widefield, and confocal microscopy, and analyzed the images. S.H., and U.M. supervised the project, designed the study, and wrote the manuscript.

### **Declaration of interests**

The authors declare no competing interests.

## References

- Arsenijevic, D., Onuma, H., Pecqueur, C., Raimbault, S., Manning, B.S., Miroux, B., Couplan, E., Alves-Guerra, M.C., Gubern, M., Surwit, R., et al. (2000). Disruption of the uncoupling protein-2 gene in mice reveals a role in immunity and reactive oxygen species production. *Nat Genet* 26, 435-439. 10.1038/82565.
- Berry, B.J., Trewin, A.J., Amitrano, A.M., Kim, M., and Wojtovich, A.P. (2018). Use the Protonmotive Force: Mitochondrial Uncoupling and Reactive Oxygen Species. *J Mol Biol* 430, 3873-3891. 10.1016/j.jmb.2018.03.025.
- Billingham, L.K., Stoolman, J.S., Vasan, K., Rodriguez, A.E., Poor, T.A., Szibor, M., Jacobs, H.T., Reczek, C.R., Rashidi, A., Zhang, P., et al. (2022). Mitochondrial electron transport chain is necessary for NLRP3 inflammasome activation. *Nat Immunol*. 10.1038/s41590-022-01185-3.
- Bouillaud, F. (2009). UCP2, not a physiologically relevant uncoupler but a glucose sparing switch impacting ROS production and glucose sensing. *Biochim Biophys Acta* 1787, 377-383. 10.1016/j.bbabi.2009.01.003.
- Brand, M.D., and Esteves, T.C. (2005). Physiological functions of the mitochondrial uncoupling proteins UCP2 and UCP3. *Cell Metab* 2, 85-93. 10.1016/j.cmet.2005.06.002.
- Bratton, D.L., and Henson, P.M. (2011). Neutrophil clearance: when the party is over, clean-up begins. *Trends Immunol* 32, 350-357. 10.1016/j.it.2011.04.009.
- Cannon, B., Shabalina, I.G., Kramarova, T.V., Petrovic, N., and Nedergaard, J. (2006). Uncoupling proteins: a role in protection against reactive oxygen species--or not? *Biochim Biophys Acta* 1757, 449-458. 10.1016/j.bbabi.2006.05.016.
- Chang, C.F., Goods, B.A., Askenase, M.H., Hammond, M.D., Renfro, S.C., Steinschneider, A.F., Landreneau, M.J., Ai, Y., Beatty, H.E., da Costa, L.H.A., et al. (2018). Erythrocyte efferocytosis modulates macrophages towards recovery after intracerebral hemorrhage. *J Clin Invest* 128, 607-624. 10.1172/JCI95612.
- Cook, D.J., Walter, S.D., Cook, R.J., Griffith, L.E., Guyatt, G.H., Leasa, D., Jaeschke, R.Z., and Brun-Buisson, C. (1998). Incidence of and risk factors for ventilator-associated pneumonia in critically ill patients. *Ann Intern Med* 129, 433-440.
- Davies, L.C., Jenkins, S.J., Allen, J.E., and Taylor, P.R. (2013). Tissue-resident macrophages. *Nat Immunol* 14, 986-995. 10.1038/ni.2705.
- Doran, A.C., Yurdagul, A., Jr., and Tabas, I. (2020). Efferocytosis in health and disease. *Nat Rev Immunol* 20, 254-267. 10.1038/s41577-019-0240-6.
- Elliott, M.R., Koster, K.M., and Murphy, P.S. (2017). Efferocytosis Signaling in the Regulation of Macrophage Inflammatory Responses. *J Immunol* 198, 1387-1394. 10.4049/jimmunol.1601520.
- Enliven Therapeutics Ltd., C.g. (2021). A Phase 2b Multi-Center, Randomized, Double-Blind, Placebo-Controlled Study, Evaluating Efficacy and Safety of Allocetra-OTS in Patients With Severe or Critical COVID-19 With Associated Acute Respiratory Distress Syndrome (ARDS). <https://clinicaltrials.gov/ct2/show/NCT04922957>.
- Faas, M., Ipseiz, N., Ackermann, J., Culemann, S., Gruneboom, A., Schroder, F., Rothe, T., Scholtyssek, C., Eberhardt, M., Bottcher, M., et al. (2021). IL-33-induced metabolic reprogramming controls the differentiation of alternatively activated macrophages and the resolution of inflammation. *Immunity* 54, 2531-2546 e2535. 10.1016/j.immuni.2021.09.010.
- Fadok, V.A., Bratton, D.L., Konowal, A., Freed, P.W., Westcott, J.Y., and Henson, P.M. (1998). Macrophages that have ingested apoptotic cells in vitro inhibit proinflammatory cytokine production through autocrine/paracrine mechanisms involving TGF-beta, PGE2, and PAF. *J Clin Invest* 101, 890-898. 10.1172/JCI1112.
- Fleury, C., Neverova, M., Collins, S., Raimbault, S., Champigny, O., Levi-Meyrueis, C., Bouillaud, F., Seldin, M.F., Surwit, R.S., Ricquier, D., and Warden, C.H. (1997). Uncoupling protein-2: a novel gene linked to obesity and hyperinsulinemia. *Nat Genet* 15, 269-272. 10.1038/ng0397-269.
- Fullerton, J.N., O'Brien, A.J., and Gilroy, D.W. (2013). Pathways mediating resolution of inflammation: when enough is too much. *J Pathol* 231, 8-20. 10.1002/path.4232.

- Gerlach, B.D., Ampomah, P.B., Yurdagul, A., Jr., Liu, C., Luring, M.C., Wang, X., Kasikara, C., Kong, N., Shi, J., Tao, W., and Tabas, I. (2021). Efferocytosis induces macrophage proliferation to help resolve tissue injury. *Cell Metab* 33, 2445-2463 e2448. 10.1016/j.cmet.2021.10.015.
- Grabiec, A.M., and Hussell, T. (2016). The role of airway macrophages in apoptotic cell clearance following acute and chronic lung inflammation. *Semin Immunopathol* 38, 409-423. 10.1007/s00281-016-0555-3.
- Green, G.M., and Kass, E.H. (1964). The Role of the Alveolar Macrophage in the Clearance of Bacteria from the Lung. *J Exp Med* 119, 167-176. 10.1084/jem.119.1.167.
- Hall, C.J., Boyle, R.H., Astin, J.W., Flores, M.V., Oehlers, S.H., Sanderson, L.E., Ellett, F., Lieschke, G.J., Crosier, K.E., and Crosier, P.S. (2013). Immunoresponsive gene 1 augments bactericidal activity of macrophage-lineage cells by regulating beta-oxidation-dependent mitochondrial ROS production. *Cell Metab* 18, 265-278. 10.1016/j.cmet.2013.06.018.
- Horckmans, M., Ring, L., Duchene, J., Santovito, D., Schloss, M.J., Drechsler, M., Weber, C., Soehnlein, O., and Steffens, S. (2017). Neutrophils orchestrate post-myocardial infarction healing by polarizing macrophages towards a reparative phenotype. *Eur Heart J* 38, 187-197. 10.1093/eurheartj/ehw002.
- Hussell, T., and Bell, T.J. (2014). Alveolar macrophages: plasticity in a tissue-specific context. *Nat Rev Immunol* 14, 81-93. 10.1038/nri3600.
- Jain, S., Self, W.H., Wunderink, R.G., Fakhran, S., Balk, R., Bramley, A.M., Reed, C., Grijalva, C.G., Anderson, E.J., Courtney, D.M., et al. (2015). Community-Acquired Pneumonia Requiring Hospitalization among U.S. Adults. *N Engl J Med* 373, 415-427. 10.1056/NEJMoa1500245.
- Kaur, M., Bell, T., Salek-Ardakani, S., and Hussell, T. (2015). Macrophage adaptation in airway inflammatory resolution. *Eur Respir Rev* 24, 510-515. 10.1183/16000617.0030-2015.
- Lowes, D.A., Thottakam, B.M., Webster, N.R., Murphy, M.P., and Galley, H.F. (2008). The mitochondria-targeted antioxidant MitoQ protects against organ damage in a lipopolysaccharide-peptidoglycan model of sepsis. *Free Radic Biol Med* 45, 1559-1565. 10.1016/j.freeradbiomed.2008.09.003.
- Matt, U., Warszawska, J.M., Bauer, M., Dietl, W., Mesteri, I., Doninger, B., Haslinger, I., Schabbauer, G., Perkmann, T., Binder, C.J., et al. (2009). Bbeta(15-42) protects against acid-induced acute lung injury and secondary pseudomonas pneumonia in vivo. *Am J Respir Crit Care Med* 180, 1208-1217. 10.1164/rccm.200904-0626OC.
- Matthay, M.A., Ware, L.B., and Zimmerman, G.A. (2012). The acute respiratory distress syndrome. *J Clin Invest* 122, 2731-2740. 10.1172/JCI60331.
- Medeiros, A.I., Serezani, C.H., Lee, S.P., and Peters-Golden, M. (2009). Efferocytosis impairs pulmonary macrophage and lung antibacterial function via PGE2/EP2 signaling. *J Exp Med* 206, 61-68. 10.1084/jem.20082058.
- Merlin, J., Ivanov, S., Dumont, A., Sergushichev, A., Gall, J., Stunault, M., Ayrault, M., Vaillant, N., Castiglione, A., Swain, A., et al. (2021). Non-canonical glutamine transamination sustains efferocytosis by coupling redox buffering to oxidative phosphorylation. *Nat Metab* 3, 1313-1326. 10.1038/s42255-021-00471-y.
- Metheny, N.A., Clouse, R.E., Chang, Y.H., Stewart, B.J., Oliver, D.A., and Kollef, M.H. (2006). Tracheobronchial aspiration of gastric contents in critically ill tube-fed patients: frequency, outcomes, and risk factors. *Crit Care Med* 34, 1007-1015. 10.1097/01.CCM.0000206106.65220.59.
- Mills, E.L., Kelly, B., Logan, A., Costa, A.S.H., Varma, M., Bryant, C.E., Tourlomousis, P., Dabritz, J.H.M., Gottlieb, E., Latorre, I., et al. (2016). Succinate Dehydrogenase Supports Metabolic Repurposing of Mitochondria to Drive Inflammatory Macrophages. *Cell* 167, 457-470 e413. 10.1016/j.cell.2016.08.064.
- Morens, D.M., Taubenberger, J.K., and Fauci, A.S. (2008). Predominant role of bacterial pneumonia as a cause of death in pandemic influenza: implications for pandemic influenza preparedness. *J Infect Dis* 198, 962-970. 10.1086/591708.
- Morgan, D.J., Casulli, J., Chew, C., Connolly, E., Lui, S., Brand, O.J., Rahman, R., Jagger, C., and Hussell, T. (2018). Innate Immune Cell Suppression and the Link With Secondary Lung Bacterial Pneumonia. *Front Immunol* 9, 2943. 10.3389/fimmu.2018.02943.

- Morioka, S., Maueroeder, C., and Ravichandran, K.S. (2019). Living on the Edge: Efferocytosis at the Interface of Homeostasis and Pathology. *Immunity* 50, 1149-1162. 10.1016/j.immuni.2019.04.018.
- Morioka, S., Perry, J.S.A., Raymond, M.H., Medina, C.B., Zhu, Y., Zhao, L., Serbulea, V., Onengut-Gumuscu, S., Leitinger, N., Kucenas, S., et al. (2018). Efferocytosis induces a novel SLC program to promote glucose uptake and lactate release. *Nature* 563, 714-718. 10.1038/s41586-018-0735-5.
- Naik, E., and Dixit, V.M. (2011). Mitochondrial reactive oxygen species drive proinflammatory cytokine production. *J Exp Med* 208, 417-420. 10.1084/jem.20110367.
- Neupane, A.S., Willson, M., Chojnacki, A.K., Vargas, E.S.C.F., Morehouse, C., Carestia, A., Keller, A.E., Peiseler, M., DiGiandomenico, A., Kelly, M.M., et al. (2020). Patrolling Alveolar Macrophages Conceal Bacteria from the Immune System to Maintain Homeostasis. *Cell*. 10.1016/j.cell.2020.08.020.
- Nubel, T., Emre, Y., Rabier, D., Chadefaux, B., Ricquier, D., and Bouillaud, F. (2008). Modified glutamine catabolism in macrophages of Ucp2 knock-out mice. *Biochim Biophys Acta* 1777, 48-54. 10.1016/j.bbabi.2007.11.002.
- Park, D., Han, C.Z., Elliott, M.R., Kinchen, J.M., Trampont, P.C., Das, S., Collins, S., Lysiak, J.J., Hoehn, K.L., and Ravichandran, K.S. (2011). Continued clearance of apoptotic cells critically depends on the phagocyte Ucp2 protein. *Nature* 477, 220-224. 10.1038/nature10340.
- Pecqueur, C., Alves-Guerra, C., Ricquier, D., and Bouillaud, F. (2009). UCP2, a metabolic sensor coupling glucose oxidation to mitochondrial metabolism? *IUBMB Life* 61, 762-767. 10.1002/iub.188.
- Peiseler, M., and Kubes, P. (2019). More friend than foe: the emerging role of neutrophils in tissue repair. *J Clin Invest* 129, 2629-2639. 10.1172/JCI124616.
- Poon, I.K., Lucas, C.D., Rossi, A.G., and Ravichandran, K.S. (2014). Apoptotic cell clearance: basic biology and therapeutic potential. *Nat Rev Immunol* 14, 166-180. 10.1038/nri3607.
- Reber, L.L., Gillis, C.M., Starkl, P., Jonsson, F., Sibilano, R., Marichal, T., Gaudenzio, N., Berard, M., Rogalla, S., Contag, C.H., et al. (2017). Neutrophil myeloperoxidase diminishes the toxic effects and mortality induced by lipopolysaccharide. *J Exp Med* 214, 1249-1258. 10.1084/jem.20161238.
- Rupprecht, A., Moldzio, R., Modl, B., and Pohl, E.E. (2019). Glutamine regulates mitochondrial uncoupling protein 2 to promote glutaminolysis in neuroblastoma cells. *Biochim Biophys Acta Bioenerg* 1860, 391-401. 10.1016/j.bbabi.2019.03.006.
- Saas, P., Daguindau, E., and Perruche, S. (2016). Concise Review: Apoptotic Cell-Based Therapies- Rationale, Preclinical Results and Future Clinical Developments. *Stem Cells* 34, 1464-1473. 10.1002/stem.2361.
- Schneider, C., Nobs, S.P., Kurrer, M., Rehrauer, H., Thiele, C., and Kopf, M. (2014). Induction of the nuclear receptor PPAR-gamma by the cytokine GM-CSF is critical for the differentiation of fetal monocytes into alveolar macrophages. *Nat Immunol* 15, 1026-1037. 10.1038/ni.3005.
- Serhan, C.N., and Savill, J. (2005). Resolution of inflammation: the beginning programs the end. *Nat Immunol* 6, 1191-1197. 10.1038/ni1276.
- Steer, J.H., Mann, T.S., Lo, S.Z., Inglis, J.J., Yap, H.S., Henry, P.J., and Joyce, D.A. (2013). Early induction of uncoupling protein-2 in pulmonary macrophages in hyperoxia-associated lung injury. *Inhal Toxicol* 25, 544-552. 10.3109/08958378.2013.810679.
- To, E.E., Erlich, J.R., Liong, F., Luong, R., Liong, S., Esaq, F., Oseghale, O., Anthony, D., McQualter, J., Bozinovski, S., et al. (2020). Mitochondrial Reactive Oxygen Species Contribute to Pathological Inflammation During Influenza A Virus Infection in Mice. *Antioxid Redox Signal* 32, 929-942. 10.1089/ars.2019.7727.
- Toussiro, E., Bonnefoy, F., Vauchy, C., Perruche, S., and Saas, P. (2021). Mini-Review: The Administration of Apoptotic Cells for Treating Rheumatoid Arthritis: Current Knowledge and Clinical Perspectives. *Front Immunol* 12, 630170. 10.3389/fimmu.2021.630170.
- Trzeciak, A., Wang, Y.T., and Perry, J.S.A. (2021). First we eat, then we do everything else: The dynamic metabolic regulation of efferocytosis. *Cell Metab* 33, 2126-2141. 10.1016/j.cmet.2021.08.001.
- van Heerden, P.V., Abutbul, A., Svir, S., Zlotnick, E., Nama, A., Zimro, S., El-Amore, R., Shabat, Y., Reicher, B., Falah, B., and Mevorach, D. (2021). Apoptotic Cells for Therapeutic Use in Cytokine Storm Associated With Sepsis- A Phase Ib Clinical Trial. *Front Immunol* 12, 718191. 10.3389/fimmu.2021.718191.

- Voll, R.E., Herrmann, M., Roth, E.A., Stach, C., Kalden, J.R., and Girkontaite, I. (1997). Immunosuppressive effects of apoptotic cells. *Nature* *390*, 350-351. 10.1038/37022.
- Vozza, A., Parisi, G., De Leonardis, F., Lasorsa, F.M., Castegna, A., Amorese, D., Marmo, R., Calcagnile, V.M., Palmieri, L., Ricquier, D., et al. (2014). UCP2 transports C4 metabolites out of mitochondria, regulating glucose and glutamine oxidation. *Proc Natl Acad Sci U S A* *111*, 960-965. 10.1073/pnas.1317400111.
- Wang, Y., Subramanian, M., Yurdagul, A., Jr., Barbosa-Lorenzi, V.C., Cai, B., de Juan-Sanz, J., Ryan, T.A., Nomura, M., Maxfield, F.R., and Tabas, I. (2017). Mitochondrial Fission Promotes the Continued Clearance of Apoptotic Cells by Macrophages. *Cell* *171*, 331-345 e322. 10.1016/j.cell.2017.08.041.
- West, A.P., Brodsky, I.E., Rahner, C., Woo, D.K., Erdjument-Bromage, H., Tempst, P., Walsh, M.C., Choi, Y., Shadel, G.S., and Ghosh, S. (2011). TLR signalling augments macrophage bactericidal activity through mitochondrial ROS. *Nature* *472*, 476-480. 10.1038/nature09973.
- Yurdagul, A., Jr., Subramanian, M., Wang, X., Crown, S.B., Ilkayeva, O.R., Darville, L., Kolluru, G.K., Rymond, C.C., Gerlach, B.D., Zheng, Z., et al. (2020). Macrophage Metabolism of Apoptotic Cell-Derived Arginine Promotes Continual Efferocytosis and Resolution of Injury. *Cell Metab* *31*, 518-533 e510. 10.1016/j.cmet.2020.01.001.
- Zhang, S., Weinberg, S., DeBerge, M., Gainullina, A., Schipma, M., Kinchen, J.M., Ben-Sahra, I., Gius, D.R., Yvan-Charvet, L., Chandel, N.S., et al. (2019). Efferocytosis Fuels Requirements of Fatty Acid Oxidation and the Electron Transport Chain to Polarize Macrophages for Tissue Repair. *Cell Metab* *29*, 443-456 e445. 10.1016/j.cmet.2018.12.004.
- Zhou, R., Yazdi, A.S., Menu, P., and Tschopp, J. (2011). A role for mitochondria in NLRP3 inflammasome activation. *Nature* *469*, 221-225. 10.1038/nature09663.
- Zorova, L.D., Popkov, V.A., Plotnikov, E.Y., Silachev, D.N., Pevzner, I.B., Jankauskas, S.S., Babenko, V.A., Zorov, S.D., Balakireva, A.V., Juhaszova, M., et al. (2018). Mitochondrial membrane potential. *Anal Biochem* *552*, 50-59. 10.1016/j.ab.2017.07.009.

## Figure legends

### Figure 1. Functional and transcriptional properties of AMs during acid aspiration and secondary bacterial infection

- (A) Experimental scheme for *in vivo* and *ex vivo* experiments
- (B) Bacterial load after different time points of acid aspiration and consecutive infection with *P. aeruginosa* (PA) *in vivo* for 3 hours (n=4/group)
- (C) PMN numbers in BALF during acid aspiration (without infection) over time (n>=3/group)
- (D) AM + MDM numbers in BALF during acid aspiration (without infection) over time (n>=3/group)
- (E) Bacterial killing capacity (*P. aeruginosa*) of AMs after different time points of acid aspiration *ex vivo* (n=3/group)
- (F-H) Bulk mRNA sequencing data of selected pro-inflammatory genes of AMs during acid aspiration +/- *P. aeruginosa* infection presented as heat-map (F), KEGG metabolic pathway analysis (G), volcano plot of OXPHOS genes generated from AMs after *P. aeruginosa* infection (left) versus 24 hours after acid aspiration + *P. aeruginosa* infection (right) (H) (n=4/group)
- (I) Oxygen consumption rate (OCR) during Mito Stress Test (extracellular flux assay) of AMs after acid aspiration *ex vivo* in response to *P. aeruginosa* for 6-8 hours; basal respiration (left), maximal respiration (middle) and full analysis for OCR (right) (n=4/group)
- (J) Extracellular acidification rate (ECAR) during Glyco Stress Test (extracellular flux assay) of AMs after acid aspiration *ex vivo* in response to *P. aeruginosa* for 6-8 hours

Data are presented as mean + SEM. \*p < 0.05, \*\*p < 0.01, \*\*\*p < 0.001, \*\*\*\*p < 0.0001, G+H significance indicated as negative log p-value

### Figure 2. AMs fail to mount mtROS in response to bacteria after acid aspiration

- (A-C) *Ex vivo* analyses of AMs after acid aspiration at indicated time-points for mtROS using MitoSox (A) cytosolic ROS using CM-H2DCFDA (B), and MMP using JC-1 (C) in response to *P. aeruginosa* (n>=4/group)
- (D) Bacterial killing of *P. aeruginosa* +/- MitoTEMPO 100µm for 1 hour after acid aspiration *ex vivo* (Control/Carrier: TPP) (n>=4/group)
- (E) IL-1β (left), IL-6 (middle), and TNF-α (right) secretion of AMs in response to *P. aeruginosa* after acid aspiration *ex vivo* (n>=4/group)
- (F) IL-10 secretion of AMs in response to *P. aeruginosa* after acid aspiration *ex vivo* (n>=4/group)

Data are presented as mean + SEM. \*p < 0.05, \*\*p < 0.01, \*\*\*p < 0.001, \*\*\*\*p < 0.0001

### Figure 3. Cell-type specific efferocytosis of PMNs precludes mtROS generation in response to bacteria in AMs

- (A) Total number of apoptotic PMNs and CD45<sup>neg</sup> cells after different time points of acid aspiration in the BALF (n>=3/group)
- (B) mtROS release of AMs after efferocytosis of apoptotic PMNs or alveolar epithelial cells (AECs) in response to *P. aeruginosa* (PA) (n=3/group)
- (C) MMP measurement in AMs after efferocytosis of PMNs or AECs in response to *P. aeruginosa* (n=4/group)
- (D) Bacterial killing capacity (*P. aeruginosa*) of AMs after efferocytosis of PMNs or AECs (n=5/group)

- (E) Bacterial killing capacity (*P. aeruginosa*) of AMs after efferocytosis of PMNs compared to control (no efferocytosis) +/- MitoTEMPO 100 $\mu$ M for 1 hour (Control/Carrier: TPP) (n=3/group)
- (F) IL-1 $\beta$  (left), IL-6 (middle), and TNF- $\alpha$  (right) secretion of AMs in response to *P. aeruginosa* after efferocytosis of PMNs or AECs (n=5/group)
- (G) IL-10 secretion of AMs in response to *P. aeruginosa* after efferocytosis of PMNs or AECs (n=5/group)

Data are presented as mean + SEM. \*p < 0.05, \*\*p < 0.01, \*\*\*p < 0.001, \*\*\*\*p < 0.0001

#### Figure 4. PMN-derived MPO mediates alterations of AM functions in response to bacteria

- (A) mtROS measurement in AMs after incubation with MPO, elastase (ELA-2), or Neutrophil gelatinase-associated lipocalin (NGAL) each 0.5 $\mu$ M for 3 hours in response to *P. aeruginosa* (n=3/group)
- (B) Confocal microscopy of AMs after treatment with MPO, nuclei were stained with DAPI, mitochondria with anti-TOM20 and MitoTracker Deep Red (left), quantification of the mean fluorescence intensity of anti-TOM20 normalized to control reflecting mitochondrial content (right) (n=4/group)
- (C) mtROS measurement in AMs after efferocytosis PMNs of WT or *Mpo*<sup>-/-</sup> mice in response to *P. aeruginosa* (n=7/group)
- (D) MMP measurement in AMs after efferocytosis of PMNs of WT or *Mpo*<sup>-/-</sup> mice (n=3/group)
- (E) Bacterial killing capacity (*P. aeruginosa*) by AMs after efferocytosis of PMNs of WT or *Mpo*<sup>-/-</sup> mice (n=4/group)
- (F) OCR of Mito Stress Test of AMs after efferocytosis of PMNs of WT or *Mpo*<sup>-/-</sup> mice in response to *P. aeruginosa* (n=4/group)
- (G) Experimental scheme for (H)
- (H) Bacterial outgrowth after instillation of apoptotic PMNs of WT or *Mpo*<sup>-/-</sup> mice and infection with *P. aeruginosa* (n=5/group)
- (I) Bacterial killing capacity (left: *K. pneumoniae*; right: *S. pneumoniae*) of AMs +/- pretreatment with MPO (n=4/group)
- (J) Assessment of mtROS production in AMs in response to *K. pneumoniae* (KP) +/- MPO (n=4/group).

Data are presented as mean + SEM. \*p < 0.05, \*\*p < 0.01, \*\*\*p < 0.001, \*\*\*\*p < 0.0001

#### Figure 5. MPO-mediated increase of UCP2 precludes mtROS release in response to bacteria

- (A) mtROS measurement in AMs in response to *P. aeruginosa* pre-treated with MPO and/or genipin (GNP) (100 $\mu$ M for 1 hour) *in vitro* (n>=3/group)
- (B) mtROS measurement in AMs in response to *P. aeruginosa* pre-treated with GNP compared to control (DMSO) 24 hours after acid aspiration *ex vivo* (n=3/group)
- (C) mtROS measurement in WT and *Ucp2*<sup>-/-</sup> AMs after efferocytosis of PMNs compared to control (no efferocytosis) in response to *P. aeruginosa* (n>=3/group)
- (D) MMP measurement in WT and *Ucp2*<sup>-/-</sup> AMs after efferocytosis of PMNs compared to control (no efferocytosis) in response to *P. aeruginosa* (n>=3/group)
- (E) Bacterial killing capacity (*P. aeruginosa*) of WT and *Ucp2*<sup>-/-</sup> AMs after treatment with MPO (n=3/group)

- (F) OCR of Mito Stress Test of WT and *Ucp2*<sup>-/-</sup> AMs after treatment with MPO in response to *P. aeruginosa* (n=4/group)
- (G) Western Blot of *Ucp2* and  $\beta$ -Actin as a loading control in AMs 24 hours after acid aspiration compared to sham (whole cell lysate) (n=4/group)
- (H) Western Blot of *Ucp2* and  $\beta$ -Actin as a loading control in AMs treated with MPO compared to control (n=5/group)
- (I) Experimental scheme for (J)
- (J) Bacterial outgrowth of *P. aeruginosa* in BALF 24 hours after acid aspiration and successive intratracheal instillation of GNP (300 $\mu$ M for 3 hours) compared to DMSO (control) *in vivo* (n>=3/group)

Data are presented as mean + SEM. \*p < 0.05, \*\*p < 0.01, \*\*\*p < 0.001, \*\*\*\*p < 0.0001

### Figure 6. UCP2-mediated alterations of AMs in response to bacteria depend on glutaminolysis

- (A) Diagram of UCP2 mediated rewiring of mitochondrial metabolism
- (B) Substrate Oxidation Stress test: Primary metabolic pathways, including glycolysis, fatty acid oxidation, glutaminolysis, TCA cycle, and OXPHOS; Pathway-specific inhibitors are highlighted in orange, corresponding enzymes in green (MPC = Mitochondrial Pyruvate Carrier; CPT-1 = Carnitine Palmitoyltransferase 1; GLS = Glutaminase), pathway substrates in blue (top left); Whole profile of Substrate Oxidation Stress Test (bottom left); Data displayed as alteration of maximal respiration in presence of pathway-specific inhibitors (UK5099 for glycolysis, etomoxir for fatty acid oxidation, BPTES for glutaminolysis) compared to respective uninhibited control in AMs treated with *P. aeruginosa* +/- MPO (n>=4/group) (right)
- (C) OCR during Mito Stress Test of AMs after pretreatment with MPO +/- BPTES (3  $\mu$ M for 1 hour) +/- *P. aeruginosa* (n=4/group)
- (D) mtROS measurement in AMs after pretreatment with MPO +/- BPTES (3  $\mu$ M for 1 hour) in response to *P. aeruginosa* (n=3/group)
- (E) IL-1 $\beta$  secretion of AMs in response to *P. aeruginosa* after efferocytosis of PMN +/- BPTES (n=4/group)
- (F) IL-10 secretion of AMs in response to *P. aeruginosa* after efferocytosis of PMN +/- BPTES (n=4/group)
- (G) mtROS measurement in AMs after pretreatment with MPO +/- EGCG (100 $\mu$ M for 1 hour) in response to *P. aeruginosa* (n=3/group)
- (H) MMP measurement in AMs after pretreatment with MPO +/- EGCG in response to *P. aeruginosa* (n>=3/group)
- (I) mtROS measurement in AMs +/- DM- $\alpha$ -KG ( $\alpha$ KG) (1mM for 1 hour) in response to *P. aeruginosa* (n=3/group)
- (J) MMP measurement in AMs +/- DM- $\alpha$ -KG ( $\alpha$ KG) in response to *P. aeruginosa* (n=3/group)
- (K) Bacterial killing capacity (*P. aeruginosa*) of AMs after pretreatment with MPO +/- GNP, +/- DM- $\alpha$ -KG (n>=3/group)

Data are presented as mean + SEM. \*p < 0.05, \*\*p < 0.01, \*\*\*p < 0.001, \*\*\*\*p < 0.0001

### Figure 7. MPO acts via UCP2 to limit bacterial control while improving efferocytosis in different macrophages across species

- (A) mtROS measurement in PMs (left) and BMDMs (right) after efferocytosis of PMNs or AECs in response to *P. aeruginosa* (n>=3/group)

- (B) Bacterial killing capacity of *P. aeruginosa* by PMs (left) and BMDMs (right) after efferocytosis of PMNs or AECs (n=3/group)
- (C) mtROS measurement in WT and *Ucp2*<sup>-/-</sup> PMs (left) and BMDMs (right) in response to *P. aeruginosa* (n=3/group)
- (D) mtROS measurement in human AMs after pre-treatment with MPO +/- GNP, +/- DM- $\alpha$ -KG (n>=4/group)
- (E) Efferocytic capacity of AMs *ex vivo*. AMs were incubated with pre-stained apoptotic PMNs 24 hours after acid aspiration compared to sham. Efferocytic capacity was then quantified by flow cytometry (n>=3/group)
- (F) Continued efferocytosis: During the first round of efferocytosis (1<sup>st</sup> round) AMs were incubated with either apoptotic PMNs or AECs compared to control (no efferocytosis) +/- *P. aeruginosa* (PA). In a second round of efferocytosis (2<sup>nd</sup> round), AMs of all conditions were then incubated with apoptotic pre-stained PMNs to determine the efferocytic capacity of AMs by flow cytometry (n=3/group)
- (G) Continued efferocytosis: During the first round (1<sup>st</sup> round) AMs were incubated with either apoptotic WT PMNs or *Mpo*<sup>-/-</sup> PMNs compared to control (no efferocytosis) or pre-treatment with MPO (0.5 $\mu$ M for 3 hours). All conditions were then stimulated with *P. aeruginosa* (PA). In a second round of efferocytosis (2<sup>nd</sup> round), AMs of all conditions were then incubated with apoptotic pre-stained PMNs to determine the efferocytic capacity of AMs (n>=3/group)
- (H) Efferocytic capacity of *Ucp2*<sup>-/-</sup> AMs. WT and *Ucp2*<sup>-/-</sup> AMs were treated each with MPO compared to control. All samples were subsequently incubated with pre-stained apoptotic PMNs. Efferocytic capacity was then quantified by flow cytometry (n>=3/group)
- (I) Efferocytic capacity of hAMs. hAMs were treated with human MPO (0.5 $\mu$ M for 3 hours) compared to control before incubating all samples with pre-stained apoptotic human PMNs. Efferocytic capacity was then quantified by flow cytometry (n>=3/group)
- (J) Experimental scheme for (K+L)
- (K) TUNEL staining depicting TUNEL-positive apoptotic cells of whole lung sections 24 hours after acid aspiration and secondary bacterial infection with *P. aeruginosa* + GNP (300 $\mu$ M for 3 hours) compared to control (DMSO). Depicted are representative images. White scale bar represents 50 $\mu$ m (left). Quantification of TUNEL-positive apoptotic cells (right) (n>=3/group)
- (L) Survival 24 hours after acid aspiration and secondary bacterial infection with *P. aeruginosa* + GNP compared to control (DMSO) (n=6/group)
- (M) Experimental scheme for (N+O)
- (N) Bacterial outgrowth in BALF 7 days after influenza infection and subsequent bacterial superinfection with *S. pneumoniae* + GNP compared to DMSO (control) (n=4/group)
- (O) Survival 7 days after influenza infection and subsequent bacterial superinfection with *S. pneumoniae* + GNP compared to DMSO (control) (n=6/group)

Data are presented as mean + SEM. \*p < 0.05, \*\*p < 0.01, \*\*\*p < 0.001, \*\*\*\*p < 0.0001

## **Supplemental Figures**

**Figure S1. Functional and transcriptional properties of AMs during acid aspiration, related to Figure 1. (A)** PMN numbers in BALF 3 hours after *P. aeruginosa* infection *in vivo* **(B)** Gating strategy to identify AMs, MDMs, and PMNs. **(C-D)** KEGG-pathway analysis of bulk mRNA sequencing data of AMs harvested 3 hours after *P. aeruginosa* infection versus 24 hours after acid aspiration + 3 hours *P. aeruginosa* infection for NF $\kappa$ B- (B) or TNF-signaling-pathway (C) (n=4/group). Data are presented as mean + SEM. \*p < 0.05, \*\*p < 0.01, \*\*\*p < 0.001, and \*\*\*\*p < 0.0001

**Figure S2. Mitochondrial reactive oxygen species-dependent alterations of AM functions after acid aspiration, related to Figure 2. (A)** Exemplary flow cytometric analysis (histogram) of Figure 2A depicting mean fluorescence signal of AMs stained with MitoSox after acid aspiration at indicated time-points in response to *P. aeruginosa* *ex vivo*. **(B)** Secretion of IL-1 $\beta$  (left), IL-6 (middle), and TNF- $\alpha$  (right) of AMs in response to *P. aeruginosa* +/- pre-treatment with MitoTEMPO 100 $\mu$ m for 1 hour (Control/Carrier: TPP) (n>=3/group). Data are presented as mean + SEM. \*p < 0.05, \*\*p < 0.01, \*\*\*p < 0.001, and \*\*\*\*p < 0.0001

**Figure S3. Cell-type specific efferocytosis of PMNs precludes mtROS generation in response to bacteria in AMs, related to Figure 3. (A)** Bacterial killing capacity (*P. aeruginosa*) of AMs harvested after different time points of acid aspiration *in vivo* and treated with concentrated BALF for 16 hours *ex vivo* (n=3/group) **(B)** Quadrant analysis of annexin V<sup>+</sup> and propidium iodide<sup>-</sup> apoptotic PMNs (top) and AECs (bottom) after incubation with staurosporine 0.2 $\mu$ M for 7 hours or 0.4 $\mu$ M for 23 hours, respectively. **(C)** Assessment of cROS production after efferocytosis of PMNs in response to *P. aeruginosa* (n=3/group). **(D)** Secretion of IL-10 after efferocytosis of PMNs or AECs (4 hours) (n=5/group). Data are presented as mean + SEM. \*p < 0.05, \*\*p < 0.01, \*\*\*p < 0.001, and \*\*\*\*p < 0.0001

**Figure S4. PMN-derived MPO mediates alterations of AM functions in response to bacteria, related to Figure 4. (A)** Assessment of cell viability using the WST-1 assay of AMs +/- MPO (0,5 $\mu$ M for 3 hours) (n=4/group). **(B)** mtROS release of AMs after efferocytosis of apoptotic PMNs or AECs in response to *S. pneumoniae* (*Spn*) (n=3/group). Data are presented as mean + SEM. \*p < 0.05, \*\*p < 0.01, \*\*\*p < 0.001, and \*\*\*\*p < 0.0001

**Figure S5. MPO-mediated increase of UCP2 precludes mtROS release in response to bacteria, related to Figure 5. (A)** Release of IL-1 $\beta$  (left), IL-6 (middle), and TNF- $\alpha$  (right) in response to *P. aeruginosa* +/- MPO and/or +/- GNP (n>=3/group). **(B)** Release of IL-10 in response to *P. aeruginosa* +/- MPO and/or +/- GNP (n>=3/group). **(C)** Transcriptional regulation of Ucp2 at different time points after acid aspiration + *P. aeruginosa* *in vivo* (Bulk mRNA sequencing) (left) and after efferocytosis with PMNs or AECs + *P. aeruginosa* *in vitro* (qPCR) (right) **(D)** Bacterial growth curves of *P. aeruginosa* in presence of GNP (100 $\mu$ m), DMSO (control), or untreated (measurement of absorbance at 600nm in technical triplicates every hour for 11 hours). Data are presented as mean + SEM. \*p < 0.05, \*\*p < 0.01, \*\*\*p < 0.001, and \*\*\*\*p < 0.0001

**Figure S6. MPO acts via UCP2 to limit bacterial control while improving efferocytosis in different macrophages across species, related to Figure 7. (A)** Assessment of MMP in PMs (left) and BMDMs (right) in response to *P. aeruginosa* +/- MPO (n>=3/group). **(B)** Assessment of cROS in response to *P. aeruginosa* +/- efferocytosis in PMs (left) and BMDMs (right) (n>=3/group). **(C)** Western Blot of Ucp2 and  $\beta$ -Actin as a loading control in PMs (left)

and BMDMs (right) +/- MPO (n=4/group). **(D)** Substrate Oxidation Stress test: Alteration of maximal respiration in presence of pathway-specific inhibitors (UK5099 for glycolysis, etomoxir for fatty acid oxidation, BPTES for glutaminolysis) compared to respective uninhibited control in PMs (left) and BMDMs (right) treated with *P. aeruginosa* +/- MPO (0.5 $\mu$ M for 3 hours) (n>=4/group). **(E)** IL-1 $\beta$  and IL-6 secretion of PMs (left) and BMDMs (right) in response to *P. aeruginosa* +/- efferocytosis (n>=3/group). **(F)** IL-10 secretion of PMs (left) and BMDMs (right) in response to *P. aeruginosa* +/- efferocytosis (n>=3/group). **(G)** Secretion of IL-1 $\beta$ , and IL-6 of human AMs in response to *P. aeruginosa* +/- MPO (n>=5/group). **(H)** Assessment of the MMP in AMs +/- MPO (n>=3/group). **(I)** Efferocytic capacity of PMs (left) and BMDMs (right). PMs and BMDMs were treated with MPO compared to control before incubating all samples with pre-stained apoptotic PMNs. Efferocytic capacity was then quantified by flow cytometry (n>=3/group) **(J)** Quantification of lung inflammation of H&E stained cryosections after acid aspiration and secondary bacterial infection with *P. aeruginosa* + GNP. Healthy (green) and inflamed (brown) areas were quantified, background (yellow) and non-lung tissue (purple) were excluded. Black scale bar represents 500 $\mu$ m (left). Analysis was performed by machine learning as outlined in the methods. The graphic depiction of data represents relative inflammation of the lung sections normalized to control (right). (n=3/group).

Data are presented as mean + SEM. \*p < 0.05, \*\*p < 0.01, \*\*\*p < 0.001, and \*\*\*\*p < 0.0001

## List of abbreviations

AEC	Alveolar epithelial cell
$\alpha$ -KG	Alpha-ketoglutarate
AM	Alveolar macrophage
BALF	Broncho-alveolar lavage fluid
BMDM	Bone-marrow derived macrophage
cROS	Cellular ROS
GNP	Genipin
IL	Interleukin
KEGG	Kyoto Encyclopedia of Genes and Genomes
<i>K. pneumoniae</i>	<i>Klebsiella pneumoniae</i>
mtROS	Mitochondrial reactive oxygen species
MPO	Myeloperoxidase
OCR	Oxygen consumption rate
OXPHOS	Oxidative phosphorylation
<i>P. aeruginosa</i>	<i>Pseudomonas aeruginosa</i>
PM	Peritoneal macrophage
PMN	Polymorphonuclear leukocyte
ROS	Reactive oxygen species
<i>S. pneumoniae</i>	<i>Streptococcus pneumoniae</i>
TNF- $\alpha$	Tumor necrosis factor- $\alpha$
WT	Wildtype

# Methods

## Animals

Female C57BL/6N wildtype mice were purchased from Charles River Laboratories at the age of 8-12 weeks. *Ucp2*<sup>-/-</sup> mice (B6.129S4-*Ucp2*<sup>tm1Lowl</sup>) were kindly provided by the laboratory of Natascha Sommer (University of Giessen, Hesse, Germany). Breeding pairs of *Mpo*<sup>-/-</sup> mice (B6.129X1-*Mpo*<sup>tm1Lus/J</sup>) had been purchased from Charles River. All mice were housed in a specific pathogen-free environment. Animal experiments were conducted according to the legal regulations of the German Animal Welfare Act (Tierschutzgesetz) and approved by the regional authorities of the State of Hesse (Regierungspräsidium Giessen) and the Institutional Commission for the Care and Use of Laboratory Animals (CICUAL), Buenos Aires, Argentina.

## Induction of acid aspiration

Mice were anesthetized with isoflurane (Sigma-Aldrich, Germany). Acid pneumonitis was induced by instillation of 50µl of 0.1M HCl intratracheally (i.t.) (Sigma-Aldrich, Germany). Sham-treated controls received 50µl of 0.9% NaCl (Braun, Germany) intratracheally (i.t.).

## Influenza infection

For *in vivo* influenza A virus infection, mice were anesthetized with isoflurane (Sigma-Aldrich, Germany). Subsequently, 100ffu (coinfection experiment with *S. pneumoniae*) of PR8 diluted in 70µl sterile PBS<sup>-/-</sup> were instilled i.t..

## Bacterial pneumonia

*P. aeruginosa*, strain PA103, was cultured in Luria broth (LB) medium (Roth) at 37°C with aeration and harvested at the mid-log phase. *S. pneumoniae* serotype 3 was cultured in Todd-Hewitt Broth (THY) containing 10% heat-inactivated FCS at 37°C mid-log phase. Inoculum was determined by serial dilutions on blood agar plates, and mice were infected with 2-3x10<sup>4</sup> colony forming units (CFU) of *P. aeruginosa* (after acid aspiration) or 30 CFU of *S. pneumoniae* (after influenza infection) instilled in 50µl NaCl 0,9% intranasally at indicated time points. Before inoculation, mice were short-term anesthetized by inhalation of isoflurane.

## Bacterial growth curve

In parallel, three cultures of *P. aeruginosa*, strain PA103, were cultured in Luria broth (LB) medium (Roth) at 37°C with aeration. The cultures were either treated with Genipin (100µm) or DMSO (control for Genipin) or left untreated (untreated control). The absorbance of 100µL of each culture was measured every hour for 11 hours in triplicates with an absorbance microplate reader at a wavelength of 600nm.

## **Primary cell harvest and culture**

All murine alveolar macrophages (AMs) were obtained from BALF. Mice were sacrificed, and the trachea was exposed, incised, and intubated with a blunt 21G cannula. BAL was performed by successively instilling seven times 1mL of cold PBS/- plus EDTA intratracheally. Recovery volume was centrifuged at 500g for 10 minutes. The supernatant was discarded while the cell pellet was resuspended in an RPMI-based medium containing 2.5% HEPES, 2% FCS, and 1% Penicillin/Streptomycin/L-Glutamine, and cultured at 37°C under 5% CO<sub>2</sub>. After cells had adhered, non-adherent cells were washed away.

Human BALF with a macrophage purity > 90% obtained from patients for diagnostic purposes was applied to isolate human alveolar macrophages (hAMs). BAL samples used were from non-smoking patients without chronic pulmonary diseases who provided written consent to the use of biomaterial using the consent form of the DZL (Deutsches Zentrum für Lungenforschung). The project was reviewed and is covered under the University of Giessen ethics committee decision (AZ 58/15) and was performed according to the appropriate regulations and the Declaration of Helsinki. BALF was centrifuged before cells were resuspended in an RPMI-based medium containing 2.5% HEPES, 2% FCS, and 1% Penicillin/Streptomycin/L-Glutamine, and cultured at 37°C under 5% CO<sub>2</sub>. After cells had adhered, non-adherent cells were washed away.

Murine peritoneal macrophages (PMs) were taken from peritoneal lavage fluid. Mice were euthanized, and the inner skin lining of the peritoneal cavity was exposed. The peritoneal lavage was performed by instilling 7-10mL of HBSS through a 27G needle intraperitoneally. The peritoneum was gently massaged before collecting the peritoneal fluid with a 23G needle with the mouse placed in a lateral decubitus position. Recovery volume was centrifuged, and the supernatant was discarded while PMs were purified according to manufacturer's instruction using a magnet purification kit by selecting F4/80<sup>+</sup> cells (Miltenyi Biotec; macrophage Isolation Kit, Mouse, Peritoneum). Finally, purified PMs were resuspended in an RPMI-based medium containing 10% FCS and 1% Penicillin/Streptomycin/L-Glutamine, and cultured at 37°C under 5% CO<sub>2</sub>.

Murine bone marrow-derived macrophages (BMDMs) were generated from femoral and tibial bone marrow. After mice had been sacrificed, femoral and tibial bones were isolated by removing attached muscles and tissue. The collected bone marrow was further passed through a 40 µm cell strainer to remove gross particles before centrifuging. The supernatant was discarded while the cell pellet was resuspended in an RPMI-based medium containing 10% FCS, 30ng/mL M-CSF, and 1% Penicillin/Streptomycin/L-Glutamine, and cultured at 37°C under 5% CO<sub>2</sub>. After cells had adhered, non-adherent cells were washed away, and cells were grown for 7d by adding fresh medium on days 3 and 5.

Murine bone marrow-derived neutrophils (PMNs) were isolated from femoral and tibial bone marrow. The cell pellet obtained from centrifuging the bone marrow was resuspended in MACS buffer to purify PMNs with a magnetic purification kit according to manufacturer's instruction (Miltenyi Biotec; Neutrophil Isolation Kit, Mouse).

### **In vitro cell culture**

Murine lung alveolar epithelial cells (AECs), MLE-12 (ATCC: CRL-2110), were grown in a T-75 cell culture flask supplemented with a DMEM-based medium containing 10% FCS, ITS (Insulin 0.005 mg/ml, Transferrin 0.01 mg/ml, Sodium selenite 30 nM), 1% Penicillin/Streptomycin/L-Glutamine at 37°C under 5% CO<sub>2</sub>.

### **qPCR**

RNA was isolated using RNeasy Micro Kit (QIAGEN) according to manufacturer's protocol. 250ng of isolated RNA was reverse-transcribed into cDNA. Quantitative PCR was performed with SYBR green I (Invitrogen) in the AB StepOnePlus Detection System (Applied Bioscience). mRNA amounts are presented as fold change normalized to b-actin expression as well as the untreated or sham control. The following primers were used: murine  $\beta$ -actin (forward primer, 5'-ATGGGAAGCCGAACATACTG-3'; reverse primer, 5'-CAGTCTCAGTGGGGGTGAAT-3') and murine Ucp2 (forward primer, 5'-AAGGGCTCAGAGCATGCAG-3'; reverse primer, 5'-TGGAAGCGGACCTTTACCAC-3').

### **Efferocytosis**

Murine bone marrow-derived PMNs were resuspended at  $5-10 \times 10^5$  cells/ml in an RPMI-based medium containing 10% FCS and 1% Penicillin/Streptomycin/L-Glutamine before 0.2  $\mu$ M staurosporine was added. The cell suspension was incubated for 6 hours at 37°C under 5% CO<sub>2</sub>. MLE-12 cells were treated with 0.4  $\mu$ M staurosporine for 24 hours at 37°C and 5% CO<sub>2</sub> in MLE cell culture medium. A subsequently performed flow cytometry-based annexin V/7-AAD staining confirmed equal amounts of apoptotic cells (75 +/- 5%) and less than 10% dead cells for both PMNs and MLE-12 cells. Finally, both cell types were centrifuged and washed twice to remove extracellular staurosporine.

For all efferocytosis experiments, three apoptotic cells (PMNs or AECs) per macrophage were added, meaning an apoptotic cell to efferocyte ratio of 3:1, and incubated for 4 hours before apoptotic cells were removed. These efferocytosis experiments refer to efferocytosis as a macrophage treatment.

For determining the efferocytic capacity of primary macrophages, i.e., their capacity to clear apoptotic cells, apoptotic PMNs were pre-incubated with 5  $\mu$ M CellTrace Calcein Red-Orange for 30 min at a cell concentration of  $1-10 \times 10^6$  cells/mL. After washing, three apoptotic cells

per macrophage were added, meaning an apoptotic cell to efferocyte ratio of 3:1, incubated for 60 minutes before apoptotic cells were removed. Macrophages were then subjected to flow cytometric analysis to quantify the fluorescence signal of CellTrace Calcein Red-Orange in macrophages. The mean fluorescence intensity correlates with the capacity of macrophages to clear apoptotic bodies (PMNs). The mean intensity signal of the control treatment was used to normalize the efferocytic capacity of each individual experiment.

Quantification of continued efferocytosis, referring to the continued clearance of apoptotic cells, was performed in a two-step model. During the first round of efferocytosis, macrophages were incubated with either apoptotic PMNs or AECs for 4 hours compared to control (no efferocytosis). In a second round of efferocytosis, macrophages of all conditions were then incubated with apoptotic pre-stained PMNs, as described above, to determine their efferocytic capacity.

### **Bacterial killing assay**

Primary macrophages were cultured for 3h before analysis. Afterward, each well was washed four times with NaCl 0,9% (Braun, Germany) to remove non-adherent cells, and RPMI medium supplemented with 2% FCS and 2.5% HEPES buffer was added afterward. *P. aeruginosa* (PA103) and *S. pneumoniae* (S23) were grown as indicated. *K. pneumoniae* (ATCC 700721) was grown at mid-log phase in LB medium. After thorough washing, bacteria were added with a multiplicity of infection (MOI) of approximately 5 (*P. aeruginosa*), 10 (*K. pneumoniae*), and 250 (*S. pneumoniae*), and both plates were incubated for 1h (*P. aeruginosa* and *K. pneumoniae*) or 10 min (*S. pneumoniae*) with antibiotic-free medium. Then both plates were washed four times again. One plate was immediately lysed with distilled water (Braun, Germany) to assess bacterial uptake. The other plate was left for an additional 1.5h (*P. aeruginosa*), 3h (*K. pneumoniae*), or 20 min (*S. pneumoniae*) and subsequently lysed to assess bacterial killing (relative to bacterial uptake). Serial dilutions of the lysate were incubated overnight on blood agar plates to quantify viable bacteria in each condition.

### **Assessment of mtROS, cROS, and MMP**

Primary macrophages were seeded with  $1.5 \times 10^5$  live cells per well in a 48-well plate (Greiner BIO-ONE, Germany). After adherence, each well was washed once with PBS, and heat-killed PA103, *K. pneumoniae*, or *S. pneumoniae* (MOI 100) was added for 6-8 hours. Subsequently, wells were washed twice, and cells were incubated with 3.5 $\mu$ M MitoSOX Red (ThermoFisher, United States) for 20 minutes for the assessment of mtROS, 10 $\mu$ M CM-H2DCFDA (Thermo Fisher Scientific) for 15 minutes for the assessment of cROS, or 7.7 $\mu$ M JC-1 (ThermoFisher) for 30 minutes for the assessment of the MMP. After washing, cells were immediately transferred to FACS tubes (pluriSelect, Germany) and stored on ice. The analysis was done

with a BD LSRFortessa and FACS Diva Software (Becton Dickinson, United States). Data were analyzed with FlowJo Version 10.6.2.

### **Mitochondrial ROS scavenging**

Mitochondrial ROS-associated bactericidal properties or cytokine release of primary macrophages were addressed by applying the mitochondrial-directed antioxidant and mtROS scavenger MitoTempo. Cells were treated with 100 $\mu$ m MitoTempo for 1 hour *in vitro*. Its lipophilic cationic carrier molecule, triphenylphosphonium (TPP), was applied as a control using the same treatment conditions.

### **Cytokine Measurements**

Primary macrophages were cultured for 3h prior to analysis and incubated with heat-killed *P. aeruginosa* (MOI 100) for 6-8 hours. Protein concentrations of selected cytokines and chemokines were measured in supernatants of macrophages using a BioPlex MAGPIX Multiplex Reader (BIO-RAD, United States) according to manufacturer's instructions. Data were analyzed with Bio-Plex Data Pro software.

### **Flow cytometry and cell sorting**

BAL was centrifuged and subsequently counted with an NC-250 NucleoCounter (ChemoMetec, Denmark). Cells were resuspended in blocking reagent (Gamunex, Grifolis, Spain) and indicated antibodies (listed in the Key Resources Table) for 30 min 4°C, cell suspensions were centrifuged again and resuspended in FACS buffer containing phosphate buffered saline, supplemented with 10% FCS, 0.1% sodium azide. Sytox live-dead staining was added immediately before analyzing a sample. For annexin V staining, cells were resuspended in annexin V binding buffer (10 mM HEPES, 140 mM NaCl, and 2.5 mM CaCl<sub>2</sub>) at a concentration of 0.25-1.0x10<sup>7</sup> cells/mL. Then, 100 $\mu$ L of the cell suspension were transferred to a 5mL FACS tube. Subsequently, 5 $\mu$ L of each Pacific Blue Annexin V and 7-AAD was added to the staining solution. The solution was vortexed gently and incubated for 15 min at room temperature in the dark. Finally, 400 $\mu$ l of Annexin V binding buffer was added. Flow cytometric analysis was done with BD LSRFortessa and BD FACSAria III cell sorter using FACS Diva Software (Becton Dickinson, United States). Data were analyzed with FlowJo Version 10.6.2. Live/dead staining was performed with Sytox Blue Pacific Blue (BioLegend) or 7-AAD.

### **Bulk sequencing**

Purified total RNA was amplified using the Ovation PicoSL WTA System V2 kit (NuGEN Technologies, Bemmell, Netherlands). Per sample, 2 $\mu$ g amplified cDNA was Cy-labeled using

the SureTag DNA labeling kit (Agilent, Waldbronn, Germany). The Cy5-labeled cDNA was hybridized overnight to 8 x 60K 60mer oligonucleotide spotted microarray slides (Agilent Technologies, design ID 074809). Hybridization and subsequent washing and drying of the slides was performed following the Agilent hybridization protocol. The dried slides were scanned at 2  $\mu\text{m}$ /pixel resolution using the InnoScan is900 (Innopsys, Carbonne, France). Image analysis was performed with Mapix 8.2.5 software, and calculated values for all spots were saved as GenePix results files. Stored data were evaluated using the R software (Team, 2007) (3.5.1) and the limma package (Ritchie et al., 2015) (3.30.13) from BioConductor (Gentleman et al., 2004). Gene annotation was supplemented by NCBI gene IDs via bioMart (Durinck et al., 2009) (accessed 2018-03-08). Mean spot signals were background corrected with an offset of 1 using the NormExp procedure on the negative control spots. The logarithms of the background-corrected values were quantile-normalized (Silver et al., 2009). The normalized values were then averaged for replicate spots per array. From different probes addressing the same NCBI gene ID, the probe showing the maximum average signal intensity over the samples was used in subsequent analyses. Genes were ranked for differential expression using a moderated t-statistic. Pathway analyses were done using gene set tests on the ranks of the t-values. Gene sets were defined according to the KEGG database (Kanehisa and Goto, 2000) (accessed 2018-03-08).

### **Extracellular flux analysis**

Real-time bioenergetics profiles of macrophages were observed by measuring oxygen consumption rate (OCR) using either Agilent Seahorse XF HS Mini or XFe96 analyzer (Seahorse Bioscience, Agilent Technologies, North Billerica, MA). Macrophages were plated on an 8-well XF HS Mini PDL and a 96-well XFe96 cell culture microplate at a density of 25,000 cells or 70,000 cells per well, respectively. After indicated treatments, extracellular flux analysis was performed as per manufacturer's instructions. In brief, cellular bioenergetics were investigated by applying an XF Mito Stress Test necessitating the sequential injection of 1.5 $\mu\text{M}$  oligomycin, 2.5 $\mu\text{M}$  carbonyl cyanide 4-(trifluoromethoxy) phenylhydrazone (FCCP) and 0.5/0.5 $\mu\text{M}$  rotenone/antimycin A. To reveal the metabolic phenotype and function of macrophages, XF Substrate Oxidation Stress Test was conducted, combining pathway-specific inhibition of the primary mitochondrial substrates with a subsequent XF Mito Stress Test. Therefore, 2 $\mu\text{M}$  UK5099, 3 $\mu\text{M}$  BPTES, 4 $\mu\text{M}$  Etomoxir, and medium only (control) were injected concomitantly in Port A of separate wells to interrogate the contribution of glycolysis, glutaminolysis, or fatty-acid oxidation to mitochondrial respiration. Each of these injections was followed by an XF Mito Stress Test as described above. The relative importance of each of the mentioned pathways for feeding mitochondrial respiration was determined by the potential of the pathway-specific inhibitors to reduce maximal mitochondrial respiration in comparison to

the uninhibited control meaning the greater the reduction of maximal respiration, the greater the cell relies on the specific pathway for fueling mitochondrial respiration and vice versa. Data were analyzed with Seahorse Analytics (Agilent)

### **Western Blot**

Macrophages were treated as indicated, detached by adding Trypsin/EDTA for 10min at 37°C/5%CO<sub>2</sub>. Cells had been centrifuged at 500g for 10min before supernatant was discarded. Subsequently, cell pellet was resuspended in lysis buffer containing 900μL NP-40 buffer, 100μL Proteinase-Inhibitor Cocktail (PIC), and 3.4μL DDT. Samples were then incubated on ice for 30min while being puls-vortexed every 5-10min. Finally, cell debris was precipitated by centrifugation at maximum speed ( $\geq 16,000g$ ) for 15min at 4°C. Protein concentration was quantified by Bradford Assay according to manufacturer's instructions. A sample volume containing 20-30μg of protein was mixed with loading buffer (900μL 4x Laemmli buffer + 100μL 2-Mercaptoethanol) in a ratio of 3:1. Samples were further boiled at 95°C for 5min before being cooled on ice again. 20-40μg of total protein per well were loaded on a gel (5-15%). The membrane was blocked at RT for 1h in 2% BSA in TBS-T 0.01%. Primary antibody solution was prepared by diluting UCP2 (D105V) Rabbit mAb 1:1000 in 2% BSA in TBS-T 0.01% and added to membrane overnight at 4°C. The membrane was washed three times with TBS-T before the secondary antibody (HRP anti-Rabbit 1:1000) was added for 1h at RT. Finally, imaging was performed. To detect the  $\beta$ -Actin loading control, the membrane was stripped for 30min at RT and subsequently incubated with primary and secondary antibody.

### **Histology**

Lungs were clipped at the trachea, perfused with 4% paraformaldehyde (PFA), removed, and fixed for 24 hours in 4% PFA followed by embedding in paraffin. Paraffin blocks were sectioned into 5-μm-thick slices and placed on glass slides. After deparaffinization, hematoxylin-eosin staining was performed.

### **TUNEL assay**

In situ nick-end labeling of nuclear DNA fragmentation was performed with a TUNEL apoptosis detection kit (DeadEnd Fluorometric TUNEL system, Promega) according to the supplier's instructions.

For the acquisition of fluorescence images of the TUNEL staining, the EVOS widefield microscope and the 10x air objective was used. Two channels were acquired per field of view. One corresponding to the emission of the TUNEL staining by setting the filter to the GFP position, and one using the transmitted light to capture the tissue brightfield image. Multiple

tiles (fields of view) were captured and then stitched with the acquisition software of the EVOS system.

Similarly, the brightfield images of the H&E staining were captured with the same EVOS microscope and used the 10x air objective again, using transmitted light and setting the camera to color mode. The whole lung slices were captured using multiple fields of view and stitching those with the acquisition software of EVOS.

### **Mitochondrial content**

Successful mitochondrial staining was confirmed by colocalization of anti-TOM20 and MitoTracker deep red staining. TOM20 is a translocase of the outer mitochondrial membrane. MitoTracker deep red contains a mildly thiol-reactive chloromethyl moiety and accumulates in mitochondria, but in addition, staining intensity might be influenced by the mitochondrial membrane potential. Therefore, mitochondrial content was finally quantified by the mean intensity of the anti-TOM20 signal.

AMs were seeded equally on precision coverslips (diameter: 10mm; thickness: #1.5H) and subsequently treated with 0.5 $\mu$ m MPO for 2.5-3h. After that, mitochondria were stained with MitoTracker deep red 100nm for 30min at 37°C/5%CO<sub>2</sub>. Cells were washed three times with PBS 1X. Cell fixation was achieved by adding 4% PFA (pH 7.4) for 10min at 37°C. Cells were then washed three times with PBS 1X. 0.1% Triton X-100 in PBS 1X was applied to permeabilize cells at RT for 15min before rinsing three times with PBS 1X. Blocking was performed by adding 5% goat serum containing 0.1% sodium azide at RT for 60min, followed by staining with anti-TOM20 recombinant rabbit monoclonal antibody at a 1:1000 dilution in 5% goat serum containing 0.1% sodium azide overnight at 4°C. The next day, cells were washed three times with PBS 1X. Goat anti-rabbit recombinant secondary antibody Alexa Fluor 555 was diluted 1:1000 in 5% goat serum containing 0.1% sodium azide and added to the cells for 1h at RT protected from light. Cells were washed three times with 1X PBS-T. Nuclei were stained with DAPI 10 $\mu$ g/mL in PBS for 10 minutes and rinsed thrice with PBS-T 1X. Coverslips were finally air-dried as well as mounted with ProLong glass antifade mountant.

Confocal images were acquired with an SP8 confocal microscope (Leica Microsystems) equipped with a white light laser (WLL) and multiple Hybrid Detectors (HyD) using the LAS X software (v3.5.7). Stained samples were scanned sequentially using a PL APO 63xOil /1.40 NA objective with a voxel size of 28x28x200nm. The pinhole was kept closed to 0.7AU, and we applied a 2x live average to eliminate the noise. For the excitation of DAPI, we used 0.1% of a 405nm laser. For the excitation of TOM20 and MitoTracker deep red, we used 4.3% of a 553nm laser line or 6.7% of a 641nm laser line, respectively, derived from a white light laser set at 50% of its nominal power. For the detection of the emitted wavelengths, we used three Hybrid detectors set at 413-550nm, 560-636nm, and 650-780nm. To measure the mean

intensity of TOM20, we acquired confocal images with a lower magnification objective (20xAir/0.75NA) to capture as many cells as possible. All acquired z-stacks were subsequently cleared computationally using the Lightning module of the LAS X software.

The mean intensity of the TOM20 marker as a surrogate marker for mitochondrial content was quantified from low magnification confocal images using ImageJ/Fiji as follows: Initially, we performed a maximum intensity projection for the acquired image stacks. The signal of the MitoTracker deep red was used to generate masks of cells upon filtering the generated projections with the median filter (radius 1.5) and thresholding using the Huang algorithm. The individual cells per field of view were marked with regions of interest (ROIs) using the “Analyse Particles” plugin of Fiji. Subsequently, the background pixel intensities of the TOM20 fluorescence channel were removed with the default thresholding algorithm, and for each cell-ROI, the mean fluorescence intensity was measured.

The number of TUNEL-positive cells was counted from the widefield fluorescence images using a custom-made Fiji macro. The raw images were thresholded, and a binary mask was generated. Using the brightfield image, the boundaries of the lung section were delineated. With the “Analyse Particles” plugin, we counted the number of TUNEL-positive cells within the tissue selection. Their number was then normalized by the total tissue area and reported as the number of cells per mm<sup>2</sup> tissue.

The inflammation of lung tissue from H&E staining of lung cryosections was calculated from the brightfield colored images with the usage of a machine learning algorithm. For this quantification, we used a custom-made Fiji macro and the pixel classification of a trained model from Ilastik software. The model had previously been trained by using representative cropped parts of the acquisitions with the usage of 4 different classes (i.e background, excluded area, healthy tissue, inflamed tissue). We used the Fiji macro to automatically open each big acquisition, call the ilastik classifier, and then quantify the classified image for the following areas: total lung tissue area, healthy tissue area, and inflamed area. Then the percentage of inflammation for each acquisition was calculated using the formula below:

$\% \text{ of inflammation} = 100 * (\text{Inflamed Tissue Area}) / (\text{Total Tissue Area})$ . Subsequently, the mean % of inflammation of each sacrificed animal was normalized by the mean % of inflammation of all the acquisitions from the group of the PBS-treated animals.

### **Statistical analysis**

For calculations of statistical significance, GraphPad Prism 9 was used. Data are presented as mean + standard error of the mean (s.e.m.). P values less than 0.05 were considered significant whereas P values more than 0.05 were considered non-significant and not indicated. The mean between two groups was analyzed using the two-sided Student’s t-test. Statistically significant differences between the means of three or more unrelated and

independent groups were compared using the One-way ANOVA test. P values were corrected by Dunnet's multiple comparisons test when comparing different groups to a control group or Tukey's multiple comparisons test when comparing all different groups with each other. The Two-way ANOVA approach was used to estimate how the mean of a quantitative variable changes according to the levels of two categorical variables. Šídák's multiple comparisons test was further applied to adjust P values. Survival distributions of two samples were followed up by a log-rank test (Mantel-Cox test).

Durinck, S., Spellman, P.T., Birney, E., and Huber, W. (2009). Mapping identifiers for the integration of genomic datasets with the R/Bioconductor package biomaRt. *Nat Protoc* 4, 1184-1191. 10.1038/nprot.2009.97.

Gentleman, R.C., Carey, V.J., Bates, D.M., Bolstad, B., Dettling, M., Dudoit, S., Ellis, B., Gautier, L., Ge, Y., Gentry, J., et al. (2004). Bioconductor: open software development for computational biology and bioinformatics. *Genome Biol* 5, R80. 10.1186/gb-2004-5-10-r80.

Kanehisa, M., and Goto, S. (2000). KEGG: kyoto encyclopedia of genes and genomes. *Nucleic Acids Res* 28, 27-30. 10.1093/nar/28.1.27.

Silver, J.D., Ritchie, M.E., and Smyth, G.K. (2009). Microarray background correction: maximum likelihood estimation for the normal-exponential convolution. *Biostatistics* 10, 352-363. 10.1093/biostatistics/kxn042.

Kuziel, W.A., et al. (1997). Severe reduction in leukocyte adhesion and monocyte extravasation in mice deficient in CC chemokine receptor 2. *Proc Natl Acad Sci U S A* 94(22), 12053–12058. 10.1073/pnas.94.22.12053.

# Resources Table

## Machines and devices

Machine or device	Identifier	Source
Anesthesia workstation	MiniHub V2.1 gas anesthesia workstation for small animals	TemSega
Flow cytometers	BD LSRFortessa	Becton Dickinson
	BD FACS ARIA III	
Microscopes	BX41 light microscope	Olympus
	EVOS M700	Thermo Fisher
	SP8 confocal microscope	Leica Microsystems
Multiplex reader	Bio-Plex MAGPIX Multiplex Reader	BIO-RAD
Seahorse	Seahorse XFe96 and XF HS Mini Analyzer	Agilent
Cell Counter	NucleoCounter NC-250	ChemoMetec
PCR System	StepOnePlus™ Real-Time PCR System	Applied Biosystems

## Mitochondrial probes

Mitochondrial probe	Identifier	Source
MitoSOX™ Mitochondrial Superoxide Indicators, for live-cell imaging	#M36008	Invitrogen by Thermo Fisher Scientific
CM-H2DCFDA (General Oxidative Stress Indicator)	#C6827	
JC-1 Dye (Mitochondrial Membrane Potential Probe)	#T3168	
MitoTracker™ Deep Red FM	#M22426	
MitoTEMPO	#SML0737	Sigma-Aldrich
Methyl-triphenylphosphoniumchlorid	#468002	

## Antibodies and fluorescent dyes

Target	Fluorochrome	Clone	Isotype	Host species	Identifier	Source
CD45	APC-Cy7	30-F11	IgG <sub>2b,κ</sub>	Rat	#103116	BioLegend
Ly6G	APC	1A8	IgG <sub>2a,κ</sub>	Rat	#127614	
CD11b	FITC	M1/70	IgG <sub>2b,κ</sub>	Rat	#101206	

CD11c	PE-Cy7	N418	Armenian Hamster IgG	Armenian Hamster	#117318	
7-AAD	7-AAD	n.a.	n.a.	n.a.	#420404	
Annexin V	Pacific-Blue	n.a.	n.a.	n.a.	#640918	
CD170/ Siglec-F	BV421	E50-2440	IgG <sub>2a,κ</sub>	Rat	#565934	BD Biosciences
n.a.	CellTrace™ Calcein Red-Orange, AM	n.a.	n.a.	n.a.	#C34851	Invitrogen
Tom20	Recombinant Alexa Fluor® 555 Anti-TOMM20 antibody	EPR1558 1-54	Alexa Fluor® 555 Rabbit IgG, mono-clonal (EPR25A)	Rabbit	#ab22129 2	Abcam
UCP2	UCP2 (D1O5V) Rabbit mAb	D1O5V	Rabbit IgG	Rabbit	#89326	Cell Signaling
β-Actin	β-Actin Antibody	n.a.	n.a.	Rabbit	#4967	

### Critical commercial assays and kits

Assay	Identifier	Source
WST-1 Assay Kit (Cell Proliferation)	#ab65473	Abcam
Seahorse XFp Cell Mito Stress Test Kit	#103010-100	Agilent
Seahorse XF Cell Mito Stress Test Kit	#103015-100	
Seahorse XFp Mito Fuel Flex Test Kit	#103270-100	
Seahorse XF Mito Fuel Flex Test Kit	#103260-100	
Bio-Plex Pro Human Cytokine 27-plex Assay	#M500KCAF0Y	BIO-RAD
Bio-Plex Pro Mouse Cytokine 23-plex Assay	#M60009RDPD	
RNeasy Micro Kit	#74004	Qiagen
Macrophage Isolation Kit (Peritoneum), mouse	#130-110-434	Miltenyi Biotec
MACSxpress® Whole Blood Neutrophil Isolation Kit, human	#130-104-434	
Neutrophil Isolation Kit, mouse	#130-097-658	

### Chemicals, peptides, and recombinant proteins

Chemical, peptide, or recombinant protein	Identifier	Source
Recombinant Mouse Myeloperoxidase Protein, CF	#3667-MP-250	R&D Systems
Recombinant Mouse M-CSF Protein, CF	#416-ML-050/CF	
Recombinant Human Myeloperoxidase Protein, CF	#3174-MP-250	
Recombinant Mouse Lipocalin-2/NGAL Protein, CF	#1857-LC-050	
Recombinant Mouse Neutrophil Elastase/ELA2 Protein, CF	#4517-SE	
HCl (hydrochloric acid solution) 0,1M 50ml	#2104	Sigma-Aldrich
Staurosporine from Streptomyces sp.	#S5921	
DMSO (dimethylsulfoxide)	#D2650-5X5ML	
Bovine Serum Albumin (BSA)	#A7030-50G	
EDTA (ethylenediaminetetraacetic acid)	#108418	Merck
PBS (phosphate-buffered saline)	#D1408-500ML	Thermo Fischer Scientific
NP-40 lysis buffer	#J60766.AP	
Genipin	#466642500	
Protease Inhibitor Cocktail	#ab65621	Abcam
2-Oxoglutar Säure-dimethylester	#349631	Sigma-Aldrich
(-)-Epigallocatechingallat	#E4143	Invitrogen
SYBR green 1	#1725124	

### Cell culture/ *in-vitro* assay media and supply

Medium or supply	Identifier	Source
FBS (Fetal Bovine Serum)	#10270-106	Life Technologies, Gibco
HBSS (hanks buffered saline solution)	#14175-053	
RPMI 1640 medium	#31870-074	
HEPES buffer (4-(2-hydroxyethyl)-1-piperazineethanesulfonic acid)	#15630080	
Seahorse XF HS mini FluxPak	#103724-100	Agilent
Seahorse XF Pro M FluxPak	#103775-100	
Penicillin – Streptomycin 500U/mL	#P0781-100ML	Sigma-Aldrich
L – Glutamine solution	#G7513	
Sodium Azide	#S2002	
HCl (hydrochloric acid solution) 0,1M 50ml	#2104	
Staurosporine from Streptomyces sp.	#S5921	
DMSO (dimethylsulfoxide)	#D2650-5X5ML	
Bovine Serum Albumin (BSA)	#A7030-50G	
LB medium	#X968.1	Carl Roth (Germany)
Todd Hewitt Bouillon	#500G	NutriSelect® Plus
Thermo Scientific™ Blood Agar (TSA with Sheep Blood) Medium	#10362223	Thermo Fischer Scientific
Insulin-Transferrin-Selenium (ITS -G) (100X)	#41400045	Gibco

## Anesthesia and in vivo experiments

Bacterial culture	Identifier	Source
Isoflurane 250ml	n.a.	Baxter (United States)
Ketaset 100mg/ml injection solution (Ketanest)	n.a.	Zoetis (United States)
Xylarium 20mg injection solution	n.a.	Ecuphar GmbH (Germany)
Mouse Intubation Pack	#000A3747	Hallowell EMC

## Bacteria and virus

Bacterial culture	Identifier	Source
<i>K. pneumoniae</i>	700721	American Type Culture Collection
<i>S. pneumoniae</i> (PN23)	PN23	Cryo stock
<i>P. aeruginosa</i> (PA103)	PA103	
<i>Influenza A Virus</i>	Mouse-adapted PR8	

## Experimental models: Organisms/strains

Organisms/strains	Genetic Background	Source
WT	C57BL/6N	Charles River
<i>Ucp2</i> <sup>-/-</sup>	B6.129S4-Ucp2tm1Lowl	Laboratory N. Sommer, Justus-Liebig-University Gießen, Germany
<i>MPO</i> <sup>-/-</sup>	B6.129X1-Mpotm1Lus/J	Charles River

## Software

Software	application	website
Biorender	Key findings/ Overview figure and figure 6A were created with Biorender.com	<a href="http://www.biorender.com">www.biorender.com</a>
GraphPad Prism (v9.5.1)	Statistics	<a href="http://www.graphpad.com">www.graphpad.com</a>
FlowJo (v10.8)	Analysis of flow cytometry data	<a href="http://www.flowjo.com">www.flowjo.com</a>
Bio-Plex Manager Software	Analysis of Multiplex data	<a href="http://www.bio-rad.com">www.bio-rad.com</a>
BD FACSDiva software (v6.1.3)	BD FACS software	<a href="http://www.bdbiosciences.com">www.bdbiosciences.com</a>
Seahorse Analytics	Analysis of Seahorse data	<a href="http://www.seahorseanalytics.agilent.com/Account/Login">www.seahorseanalytics.agilent.com/Account/Login</a>

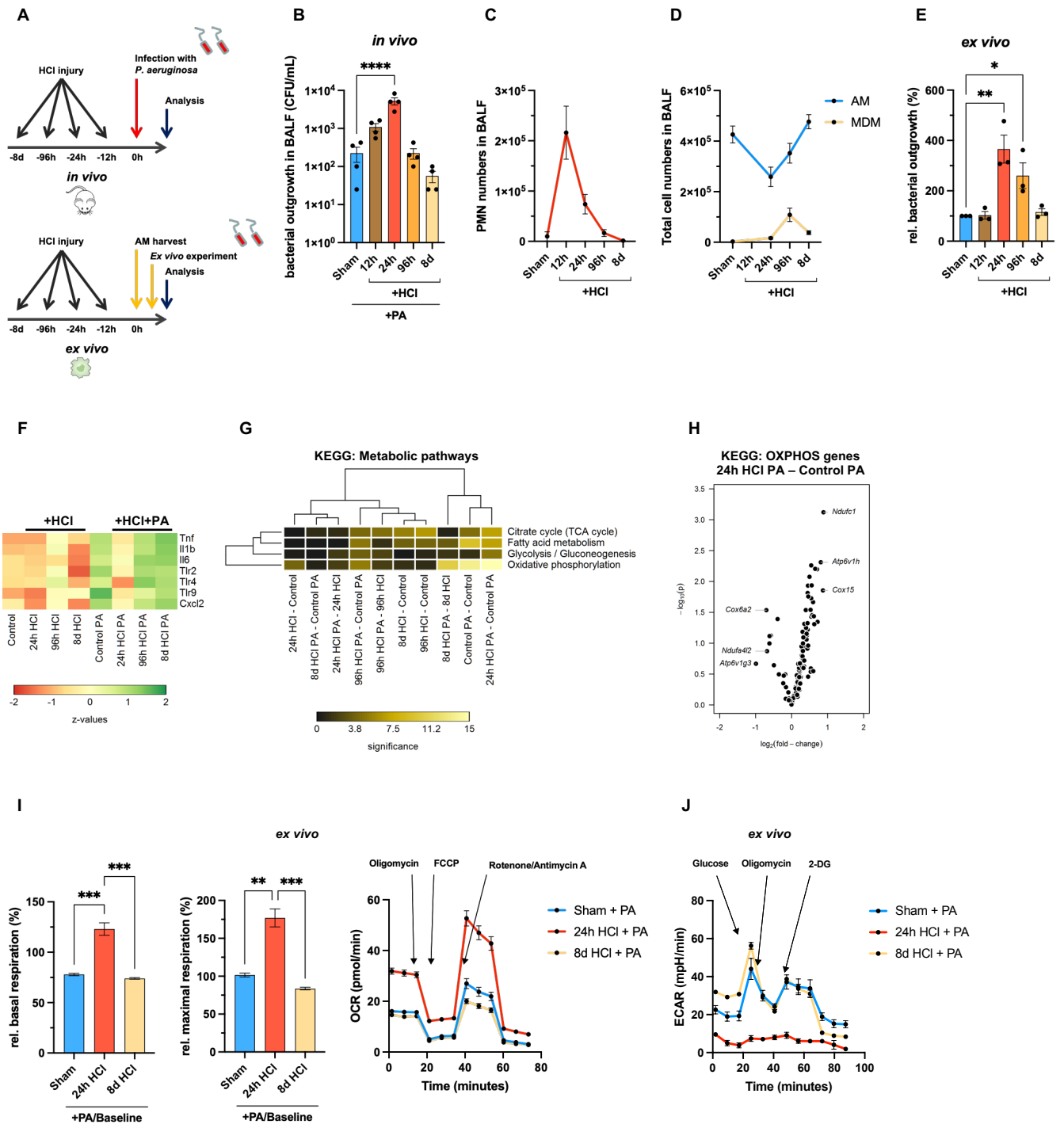


Figure 1

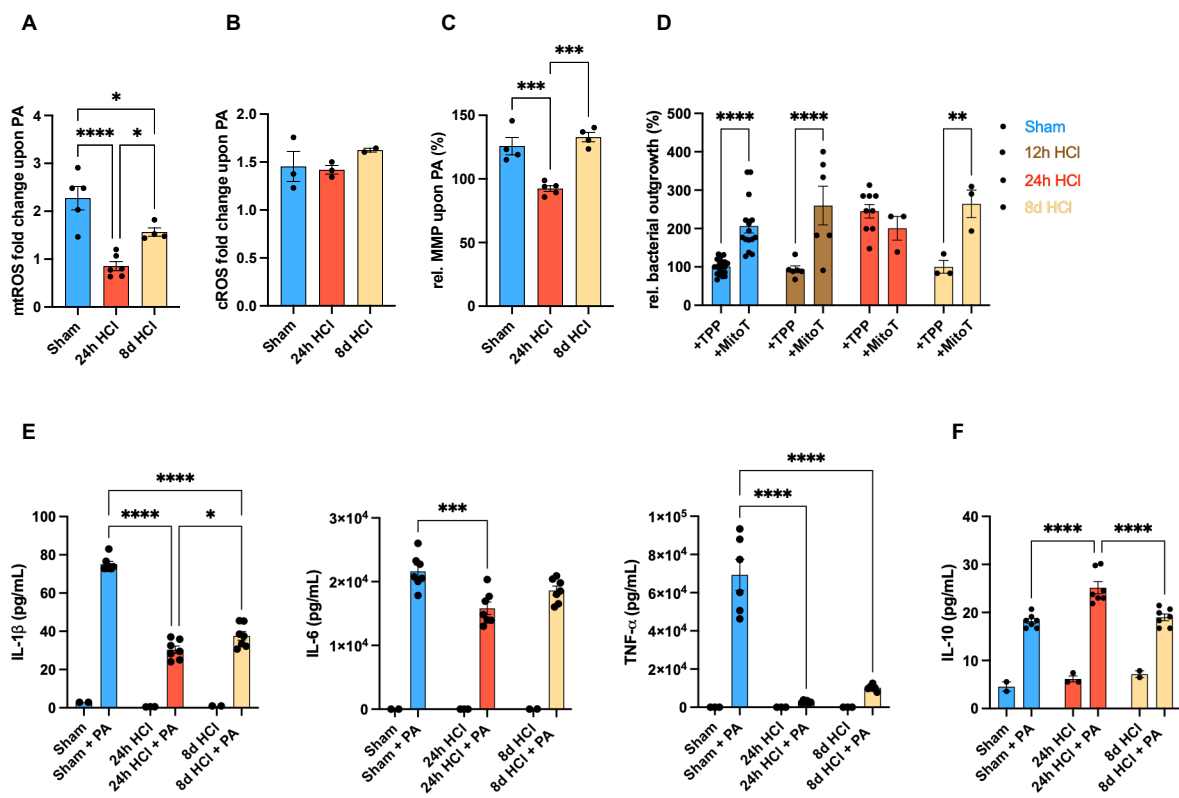


Figure 2

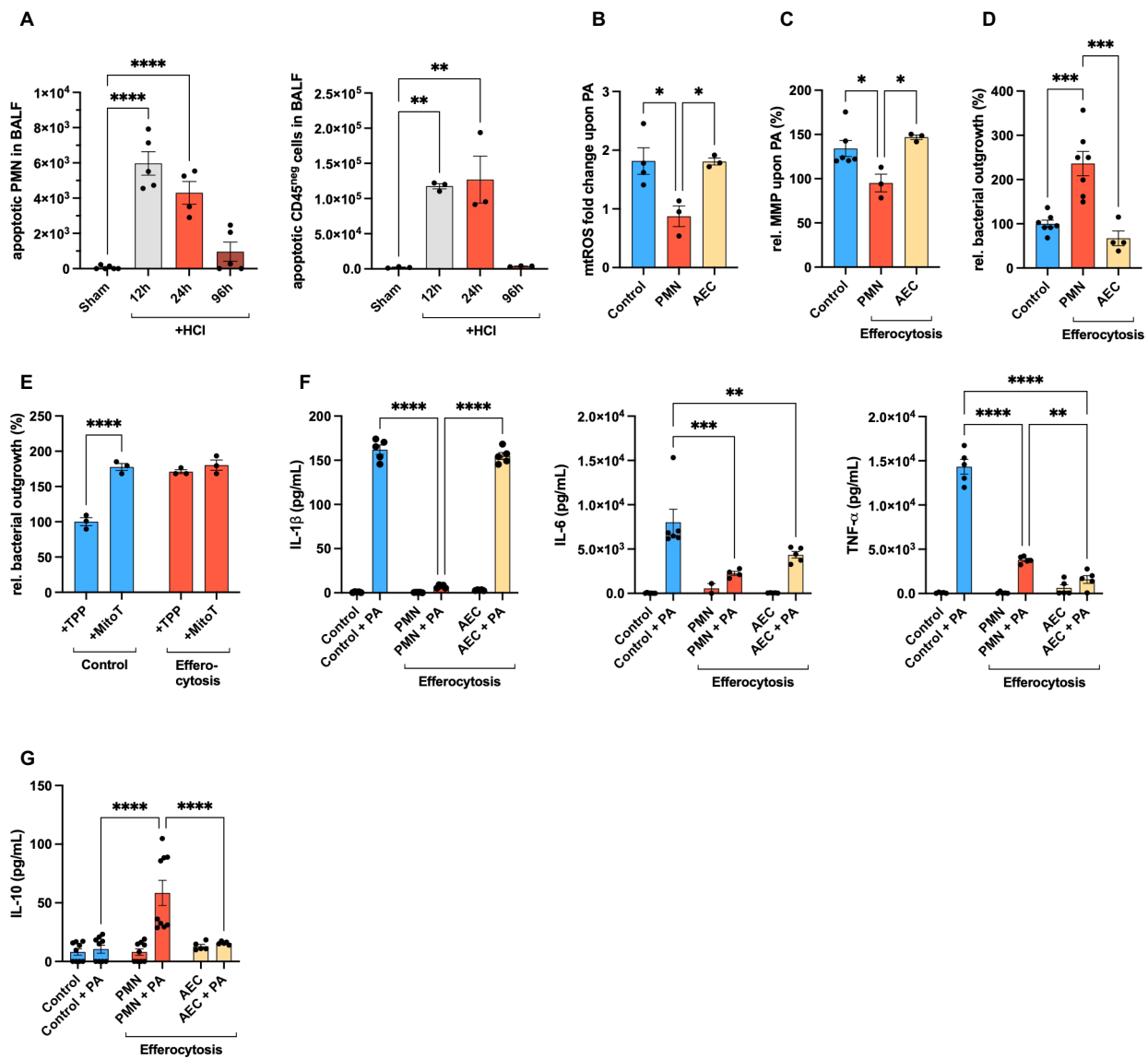


Figure 3

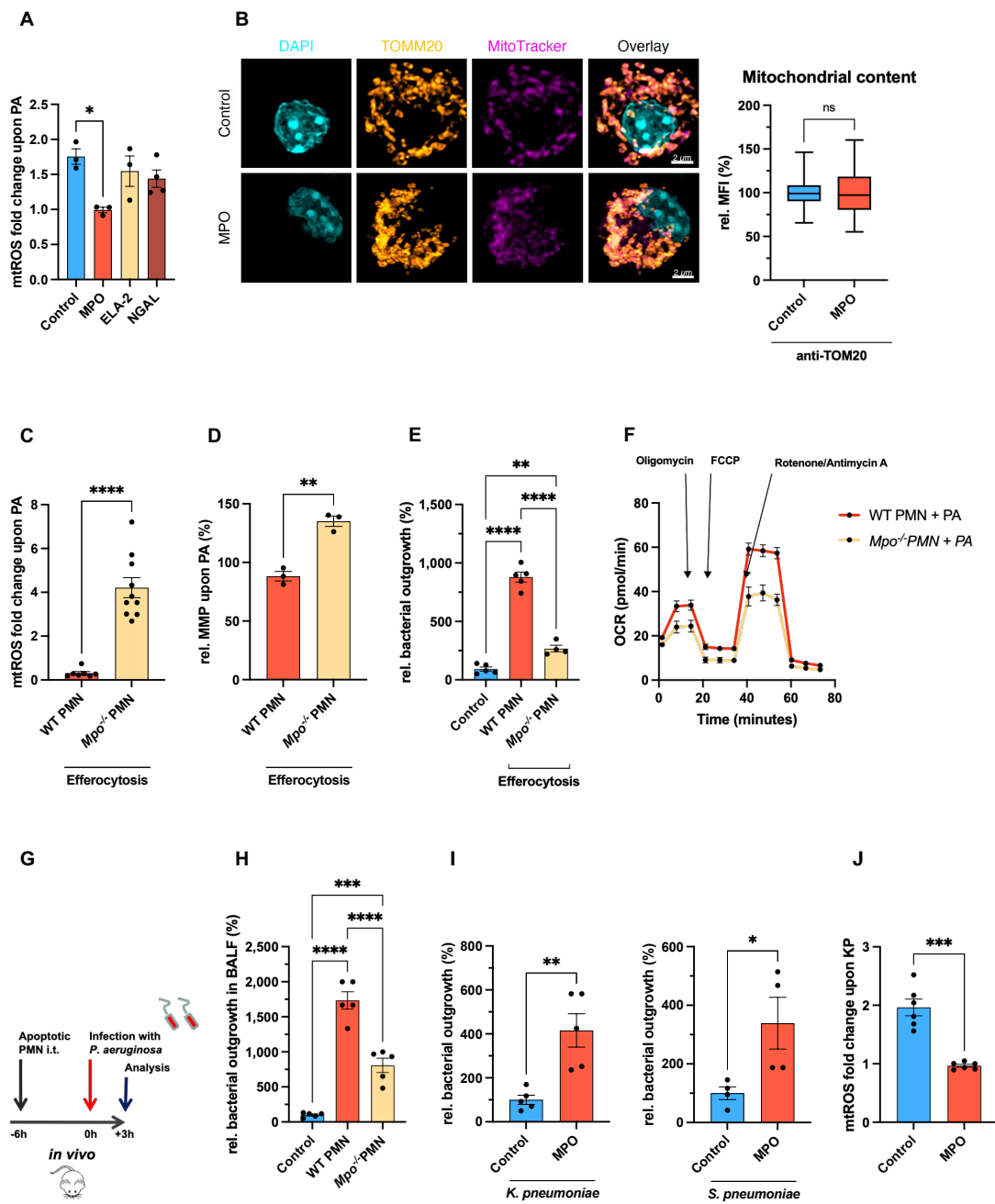


Figure 4

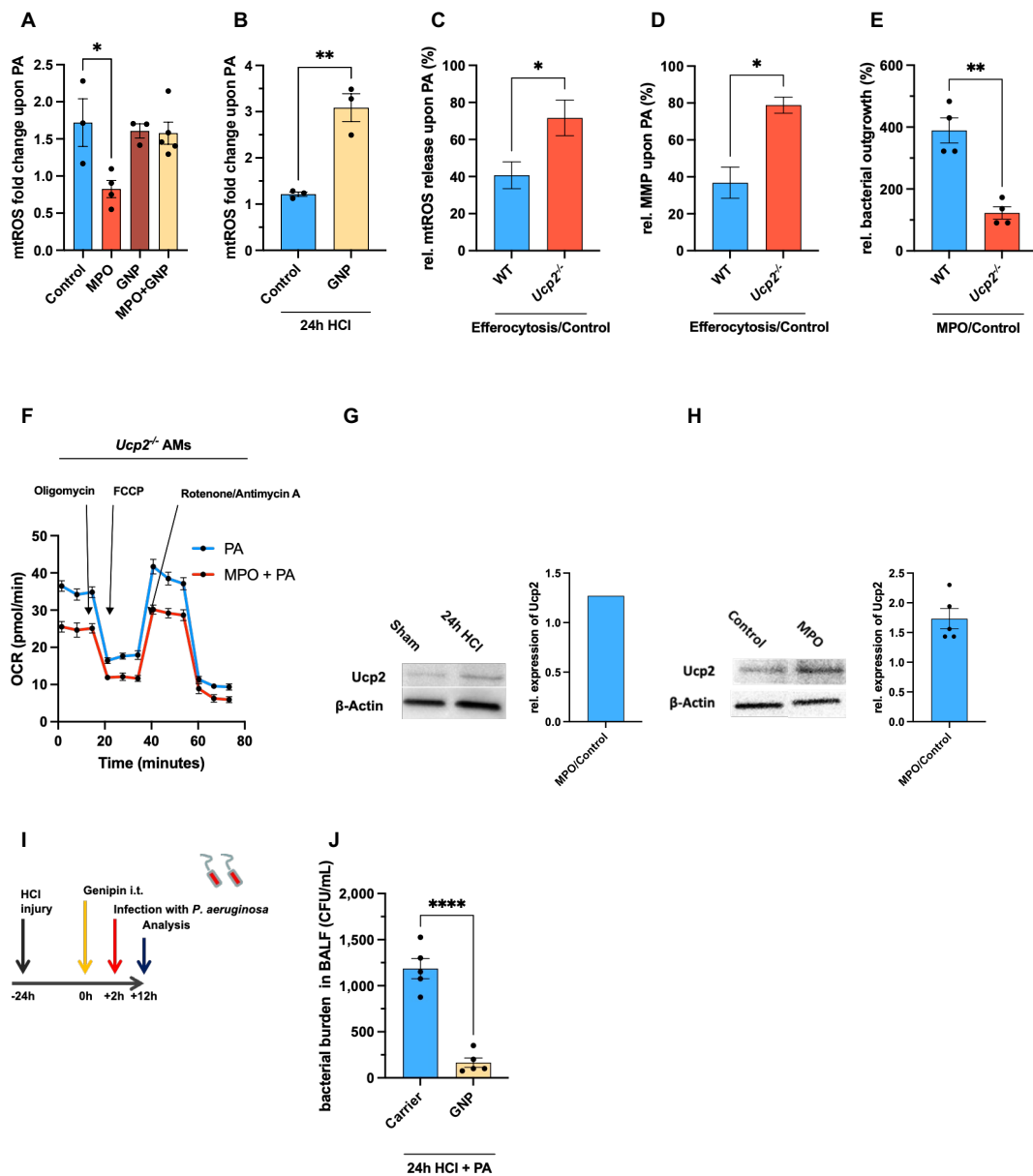


Figure 5

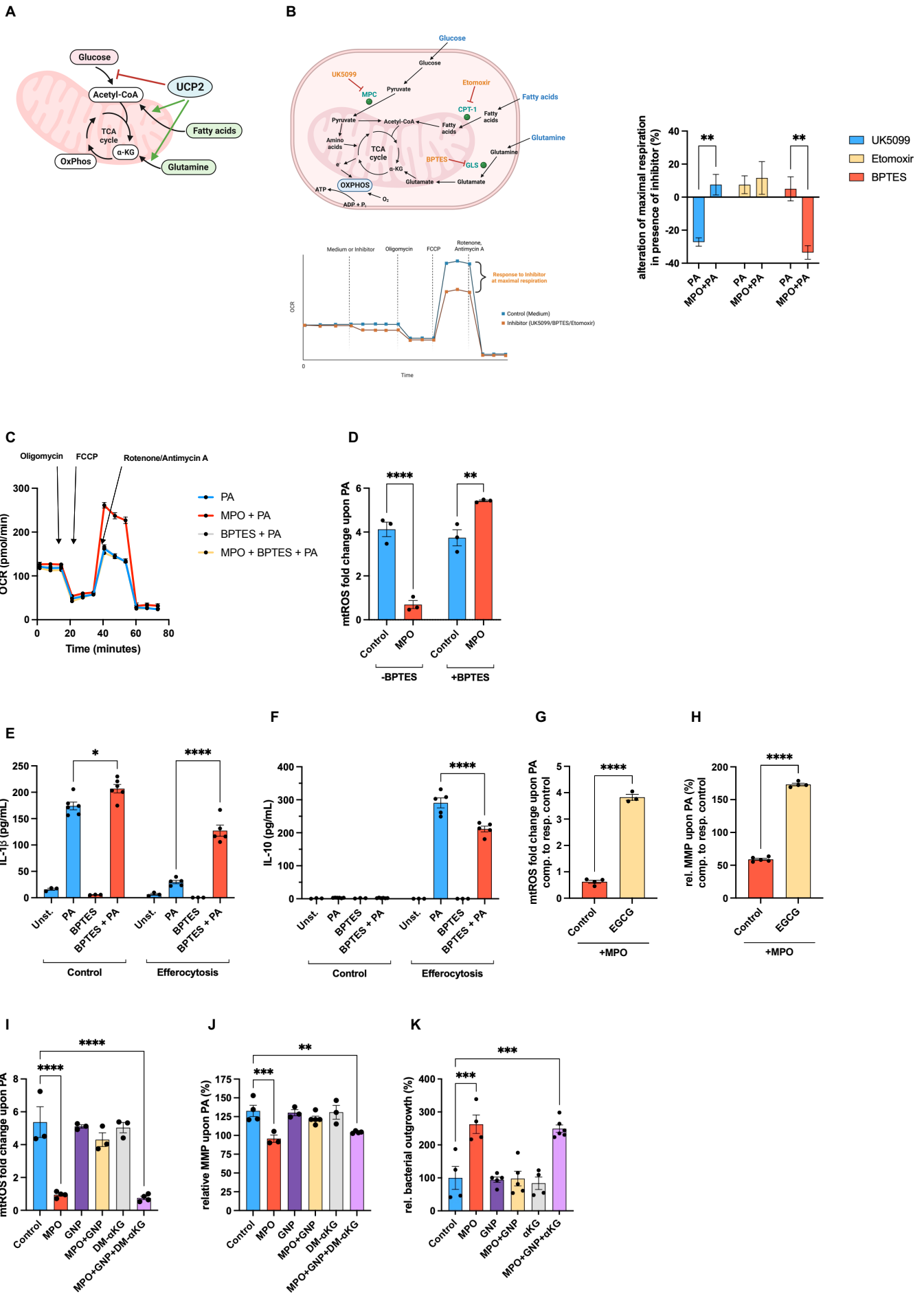


Figure 6

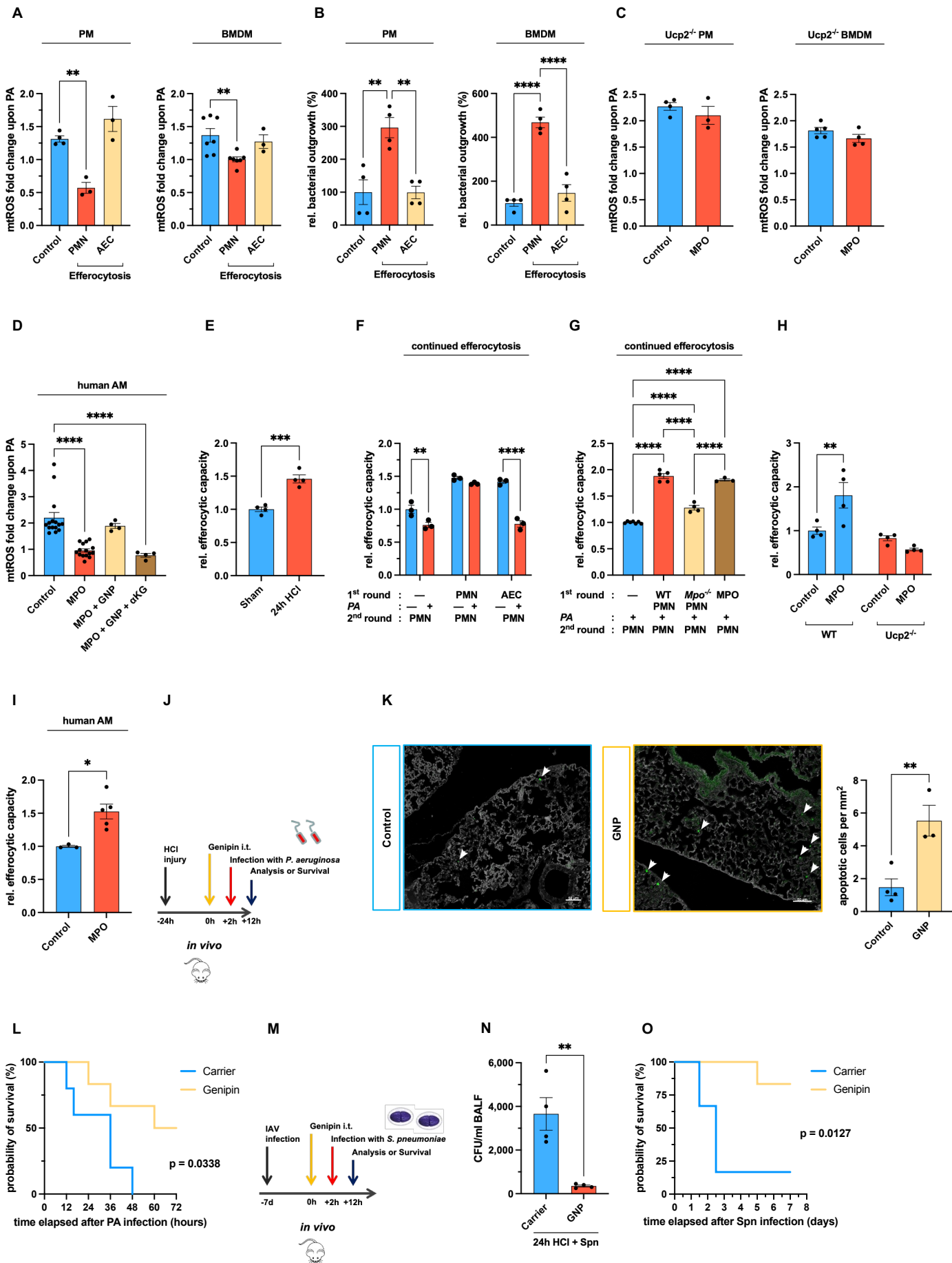


Figure 7

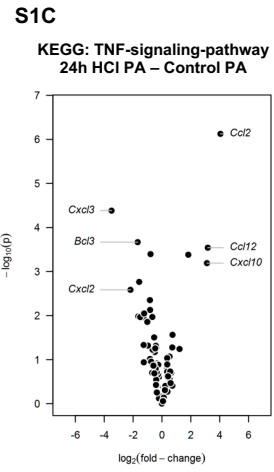
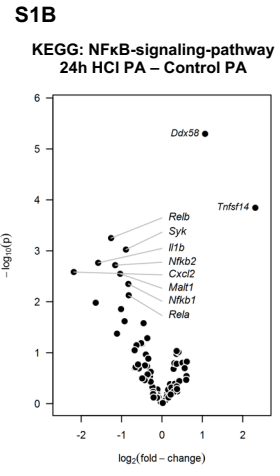
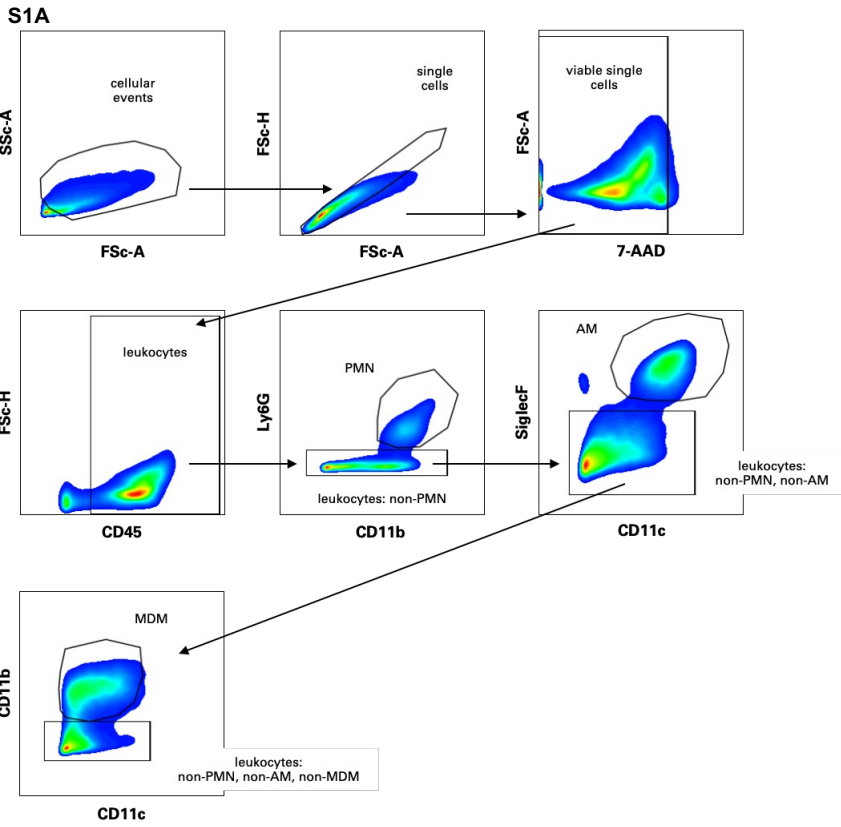


Figure S1

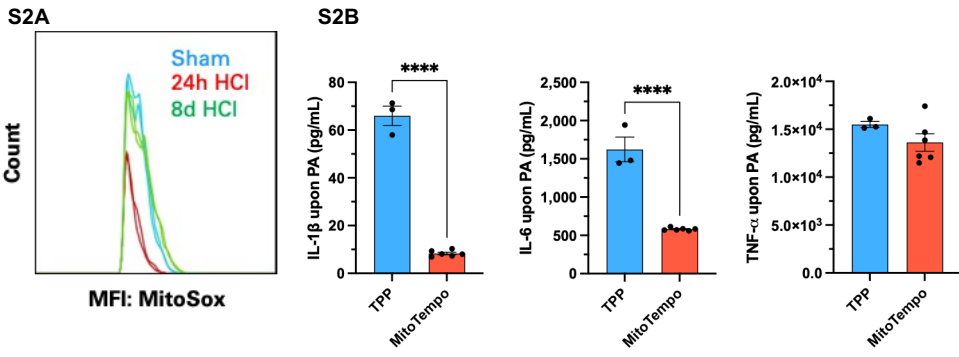


Figure S2

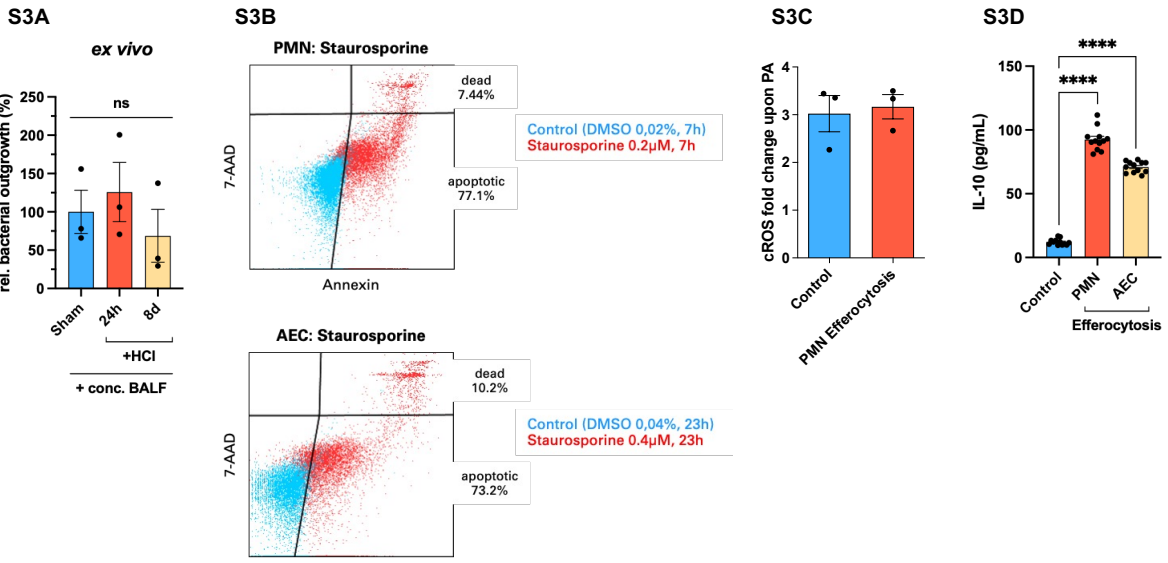
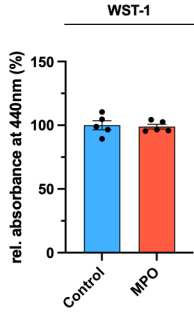


Figure S3

S4A



S4B

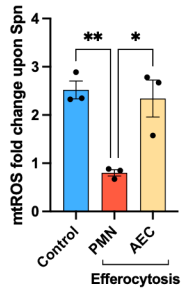


Figure S4

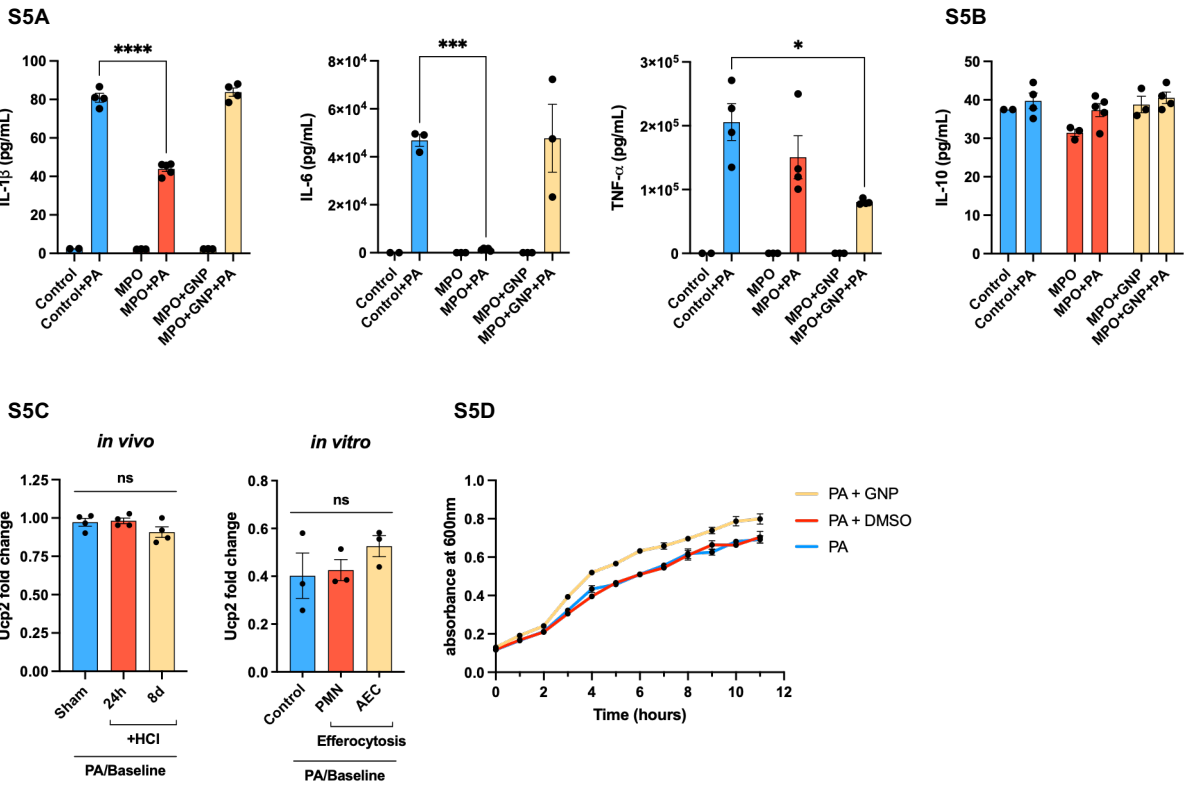


Figure S5

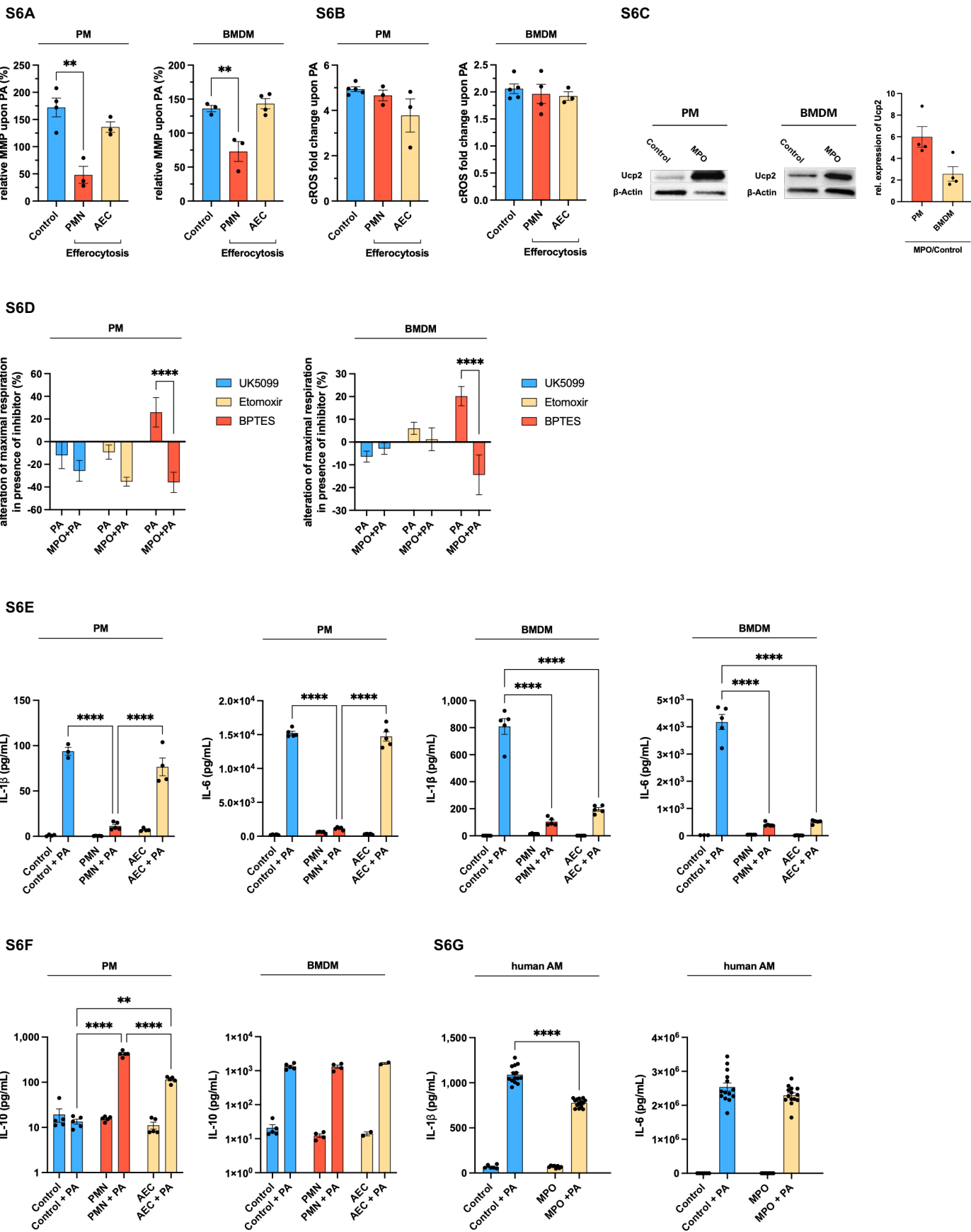
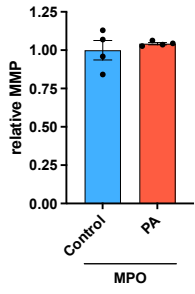
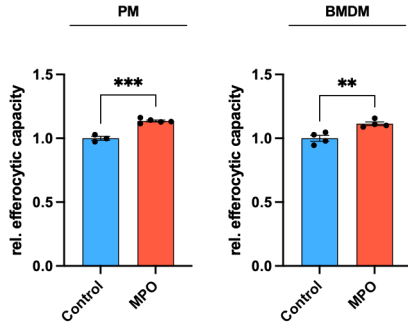


Figure S6 (1)

S6H



S6I



S6J

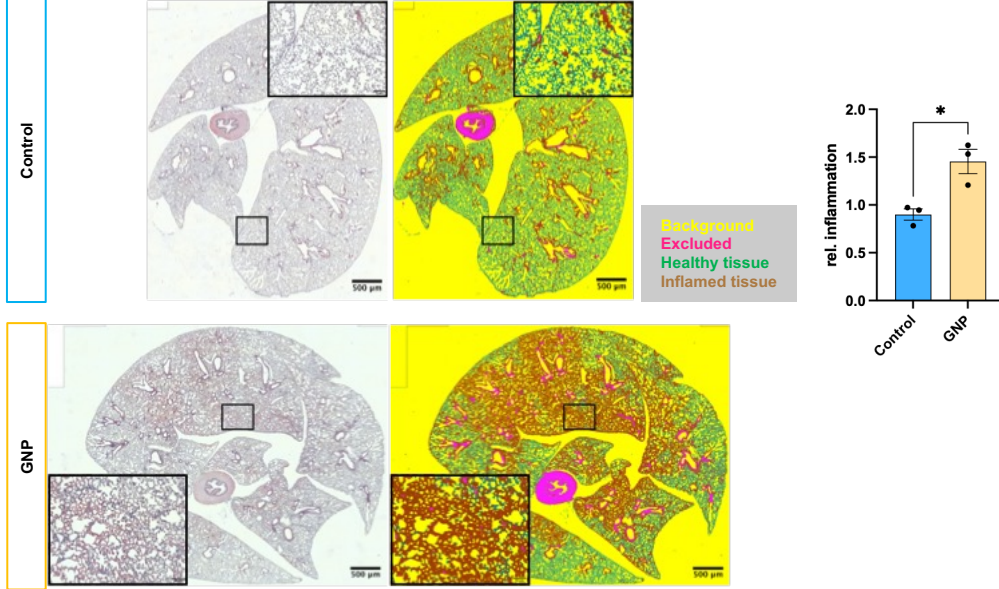


Figure S6 (2)